AC DATA ANALYSIS OF SOLID ELECTROLYTES
FINAL VERSION 3/7/13

Ian M. Hodge
School of Physics and Astronomy (retired)
Rochester Institute of Technology
Rochester, New York 14623

ABSTRACT

Mathematical techniques for analyzing the ac conductivity of ionic conductors are reviewed, with emphasis placed on solid electrolytes, and intergranular and other interfacial effects. Methods for determining the limiting low frequency conductivity in the absence of a conductivity plateau are described and illustrated with specific examples from the literature. Electrical relaxation properties of bulk solid electrolytes, and the determination of average resistive and capacitive components of intergranular and other interfacial impedances, are described. A novel method for analyzing the dielectric Maxwell-Wagner effect is described. Elementary complex number algebra and its application to ac circuits, and to dielectric and conductivity relaxation phenomenology, are briefly reviewed.

PROLOGUE

This paper was written many years ago (about 1977) as a summary of what this author knew at the time about the mathematical analysis of impedance spectroscopic data on solid electrolytes. For a variety of reasons it was never published, but inquiries and comments received since it was circulated around the solid electrolyte community led me to believe that the paper was much more useful to workers in the field than I had imagined. It seems appropriate to post it now because of continuing scientific interest in the area, and because computer interfaced impedance analyzers have become commonplace and generate data that are in a convenient form for further mathematical analysis. Because of the paper's history, the references are not recent. However, since only mathematical tools are reviewed, and these mathematical techniques have not changed with time, it was not considered important to update the examples.

I have changed the phase convention in the original paper, used by electrical engineers, in order to conform to the convention used by mathematicians and scientists. The difference conventions arise from the use of different complex exponentials: $\exp(+j\omega t)$ by engineers and $\exp(-i\omega t)$ by everyone else. Thus $+j$ in the original paper is replaced by $-i$ in this revised version, resulting in differences in the signs of the imaginary components of complex functions. The difference only determines whether the current lags the voltage, or vice versa, for a pure capacitance and is unimportant for the material discussed here. The change was made to establish consistency with scientific conventions.

Some errors in the original manuscript have been corrected, and the clarity of presentation has been improved in places.

I also introduce a nomenclature that is intended to dispel a common source of confusion about uses of the electric modulus. Conductivity and dielectric relaxations are observed separately in the same system only when the conductivity relaxation occurs at a lower frequency than the dielectric one – otherwise the dielectric loss from the limiting low frequency conductivity overwhelms all dielectric relaxation information. The symbol ε_∞ is used to denote the high frequency limit of the real part of the relative permittivity for a conductivity relaxation, which is unfortunate because it can be, and is, confused with the high frequency limit of the real part of the relative permittivity for a dielectric relaxation. We introduce a nomenclature for the distinguishing the limiting frequency values of dielectric and conductivity relaxation functions: the dielectric low frequency limit is denoted by the subscript *U* and the high frequency dielectric limit by the subscript *R*. For conductivity relaxation functions the original nomenclature is used: the subscript 0 denotes low frequency limits and the subscript ∞ denotes high frequency limits. The proposed nomenclature is illustrated in Figure A3, in which the equality $\varepsilon_\infty = \varepsilon_U$ is shown.

1. *INTRODUCTION*

Solid electrolytes have been a continuing subject of research ever since the discovery of the extraordinarily high ionic conductivity of sodium beta alumina in 1967 [1]. This interest has in large part been driven by applications to high energy density batteries. There has been a parallel development of mathematical formalisms for the analysis of ac data, that are assuming increasing importance as automated impedance analyzers become more common. Applications of these formalisms to solid electrolytes are the subject of this review.

The large electrical conductivity of solid electrolytes demands a mathematical description that differs from that used in dielectric relaxation. The distinction is important, because the use of an inappropriate formalism can result in a substantial loss of information. For example, the limiting low frequency conductivity can often only be determined, in the absence of a conductivity plateau, if an appropriate complex impedance function such as the resistivity or electric modulus is used. Formalisms that are suited to conductivity analyses are also useful for analyzing interfacial effects in dielectric media, such as the Maxwell-Wagner effect. The analysis of interfacial polarization phemomena provides a good illustration of the importance of using the correct formalisms to extract the maximum amount of information from experimental data, and this is explored at length using specific applications to literature data.

The review is divided into five sections. Following this introduction, the second section summarizes elementary complex variable algebra and its application to simple ac circuits. The third section treats dielectric relaxation from a phenomenological viewpoint, and relates it to the circuit theory of the second section. Section Four extends the dielectric phenomenology to conductivity relaxation in solid electrolytes, and introduces the formalisms that are particularly suited to its analysis. Section Five is devoted to illustrating these formalisms using experimental data from the literature, although no attempt is made to review experimental data *per se*. The properties of distribution functions are summarized in Appendices, including empirical equations for extracting distribution function parameters from loss spectra.

Several topics are excluded for the sake of brevity. The large field of electrode kinetics is omitted – it is usually assumed that the applied potential is below the decomposition potential of the electrode-electrolyte combination being studied, so that Faradaic impedances can be neglected. Thus blocking electrodes will usually be assumed, although a few exceptions are made to illustrate specific points.

The SI system of units is used throughout.

2. *COMPLEX NUMBERS and AC CIRCUITS*

2.1 *Complex Numbers.*

A complex number, z, is a number pair whose components are termed the real, x, and imaginary, y:

$$z = x + iy\,, \tag{1}$$

where $i = (-1)^{1/2}$. Thus, for example,

$$z^2 = (x^2 + y^2) + i(2xy)\,. \tag{2}$$

A function that is central to the application of complex numbers to relaxation phenomena is the complex exponential function

$$\exp(z)=\exp(x+iy)=\exp(x)\exp(y)=\exp(x)\exp\left[\cos(y)+i\sin(y)\right] \tag{3}$$

where the Euler relation for $\exp(iy)$ has been used:

$$\exp(iy)=\cos(y)+i\sin(y). \tag{4}$$

The cosine function of the real variable, *y*, can therefore be written as

$$\cos(y)=\mathrm{Re}\left[\exp(i\,z)\right] \tag{5}$$

and the sine function as

$$\sin(y)=\mathrm{Re}\left[-i\exp(i\,z)\right], \tag{6}$$

where Re denotes the real component of a complex function. Since the sine and cosine functions differ only by the phase angle $\pi/2$, eqs (5) and (6) demonstrate that *i* shifts the phase angle by $\pi/2$. The usefulness of complex numbers in describing physical properties that are measured with sinusoidal varying excitations derives from this property of *i*.

2.2 *Analytical Functions of a Complex Variable.*

Of all the possible functions of a complex variable, only one kind is useful for describing physical properties. These are the analytical functions, defined as being single valued and uniquely differentiable, the latter meaning that differentiation with respect to *z* does not depend on the direction of differentiation in the complex plane (for an excellent account of the applications of complex numbers, see reference [3]). Thus differentiation parallel to the *x* axis $(\partial/\partial x)$ produces the same result as differentiation parallel to the *y* axis $(\partial/\partial y)$, and this results in the real and imaginary parts of an analytical function being related to one another. For example, the Cauchy-Riemann relations (included here for the sake of completeness), for an analytical function *f(z)* expressed as

$$f(z)=f(x+iy)=u(x,y)+iv(x,y) \tag{7}$$

are

$$\left(\frac{\partial u}{\partial x}\right)=\left(\frac{\partial v}{\partial y}\right) \tag{8}$$

and

$$\left(\frac{\partial u}{\partial y}\right) = -\left(\frac{\partial v}{\partial x}\right). \tag{9}$$

The exponential function conforms to the Cauchy-Riemann conditions and is therefore analytical. Equations (8) and (9) reveal that *u* and *v* are harmonic functions, because they obey the two dimensional Laplace equations

$$\nabla^2 u = \nabla^2 v = 0\,. \tag{10}$$

Integral versions of the Cauchy-Riemann conditions are known as the Hilbert relations (derived from the Cauchy theorem that need not concern us here):

$$u(z) = \frac{1}{\pi}\int_{-\infty}^{+\infty} \frac{v(\omega)\,d\omega}{(\omega - z)} \tag{11}$$

$$v(z) = -\frac{1}{\pi}\int_{-\infty}^{+\infty} \frac{u(\omega)\,d\omega}{(\omega - z)} \tag{12}$$

These, together with the crossing relations (13) below, yield the Kronig-Kramers dispersion formulae. The crossing relations are

$$u(x) = u(-x)$$

and (13)

$$v(x) = -v(-x),$$

where *x* is real. Insertion of these relations into the Hilbert relations, in order to eliminate integration over a negative real argument (e.g. frequency), gives the Kronig-Kramers relationships

$$u(x) = \frac{2}{\pi}\int_{0}^{+\infty} \frac{\omega v(\omega)\,d\omega}{\left(\omega^2 - x^2\right)} \tag{14}$$

$$v(x) = \frac{2x}{\pi}\int_{0}^{+\infty} \frac{u(\omega)\,d\omega}{\left(x^2 - \omega^2\right)} \tag{15}$$

2.3 Elementary AC Circuits

Sinusoidally varying voltages and currents are fundamental to impedance spectroscopy, making complex numbers and the complex exponential function especially useful for describing them. Consider for example a sinusoidally varying voltage $V = V_0 \cos(\omega t)$ that is applied across a resistance, R_p, in parallel with a capacitance, C_p. The current through the resistance, I_R, is given by

$$I_R = \frac{V}{R_p} = \frac{V_0 \cos(\omega t)}{R_p} = V_0 G_p \cos(\omega t) = \mathrm{Re}\left[V_0 G_p \exp(-i\,\omega t) \right] , \tag{16}$$

where $G_p \equiv 1/R_p$. The current through the capacitance, I_C, is given by

$$\begin{aligned} I_C &= \frac{dq_C}{dt} = C_p \frac{dV}{dt} = -V_0\, \omega C_p \sin(\omega t) = \mathrm{Im}\left[V_0\, \omega C_p \exp(-i\,\omega t) \right] \\ &= \mathrm{Re}\left[-i V_0\, \omega C_p \exp(-i\,\omega t) \right], \end{aligned} \tag{17}$$

where q_C is the charge on the capacitor. Thus the total current is

$$I = I_R + I_C = V_0\, G_p\, \cos(\omega t) - V_0\, \omega C_p \sin(\omega t) = \mathrm{Re}\left[\left(G_p - i\,\omega C_p \right) V_0 \exp(-i\,\omega t) \right] . \tag{18}$$

The phase relations for the current can therefore be expressed by defining the parallel resistance and capacitance either as a complex admittance, A^*, given by

$$A^* = \left(G_p - i\,\omega C_p \right) = -i\omega \left(C_p - \frac{G_p}{i\omega} \right) , \tag{19}$$

or a complex impedance Z^* given by

$$Z^* = \frac{1}{A^*} = \frac{1}{\left(G_p - i\,\omega C_p \right)} = \frac{G_p}{\left(G_p^2 + \omega^2 C_p^2 \right)} + \frac{i\,\omega C_p}{\left(G_p^2 + \omega^2 C_p^2 \right)} . \tag{20}$$

Equation (20) can be rewritten as

$$Z^* = \frac{R_p}{\left(1 + \omega^2 \tau_D^2 \right)} + \frac{i\,\omega R_p\, \tau_D}{\left(1 + \omega^2 \tau_D^2 \right)} , \tag{21}$$

where

$$\tau_D = R_p C_p = C_p / G_p \tag{22}$$

is the Maxwell relaxation time [4]. The reason for the subscript D is given below. When normalized by the cell constant, k (dimensions m^{-1} from the effective electrode spacing divided by the effective electrode area), the quantities A^* and Z^* become the complex

conductivity, $\sigma^* = k \cdot A^*$, and complex resistivity, $\rho^* = Z^*/k$. The complex capacitance is given by

$$C^* = \frac{A^*}{-i\omega} = C_p + \frac{i G_p}{\omega} \ . \tag{23}$$

3 *FUNDAMENTALS OF DIELECTRIC RELAXATION*

3.1 *General Concepts and Basic Formalisms*

A freely rotating dipole in a sinusoidally varying electric field, whose angular frequency is sufficiently low that the dipole can keep up with the field, behaves as a pure capacitance, C_p. The current therefore lags behind the field by $\pi/2$ radians, and the complex admittance is given by

$$A^* = -i\,\omega C_p \, . \tag{24}$$

If the dipole cannot keep up with the field (because of friction with the molecular environment), its rotation will lag by an additional angle δ and a component of the current appears in phase with the voltage. Then eq. (17) is replaced by

$$\begin{aligned} I_c &= -V_0\,\omega C_p \sin(\omega t + \delta) \\ &= -V_0\,\omega C_p \left[\cos(\omega t)\sin(\delta) + \sin(\omega t)\cos(\delta)\right] \\ &= \mathrm{Re}\left\{-i V_0\,\omega C_p \left[\cos(\delta) - i\sin(\delta)\right]\exp(-i\,\omega t)\right\}. \end{aligned} \tag{25}$$

Comparing eq. (25) with eqs. (18) and (19) reveals that

$$C^* = C_p \cos(\delta) + i\,C_p \sin(\delta) = C' + i\,C'' \, . \tag{26}$$

Equation (23) then implies

$$G_p\,(\text{effective}) = \omega C_p \sin(\delta) \tag{27}$$

and

$$C_p\,(\text{effective}) = C_p \cos(\delta) \, . \tag{28}$$

Note that at low frequencies, when the lag angle δ tends to zero, the effective capacitance equals C_p and $G_p = 0$, as must be. When normalized by the geometric capacitance associated

with the cell constant k, $C_0 = \frac{\mathrm{e}_0}{k}$, where e_0 is the vacuum permittivity $\left(8.854\times10^{-12}\right)\mathrm{F\,m^{-1}}$, the complex capacitance becomes the complex permittivity, $\varepsilon^* = \frac{C^*}{C_0}$, so that

$$\varepsilon^* = \varepsilon' + i\,\varepsilon'' \tag{29}$$

where

$$\varepsilon' = \frac{C_p}{C_0}\left(\varepsilon_0 - \varepsilon_\infty\right)\cos\left(\delta\right) + \varepsilon_\infty, \tag{30}$$

$$\varepsilon'' = \frac{G_p}{\omega C_0} = \frac{\sigma}{e_0\omega} = \frac{C_p}{C_0}\left(\varepsilon_0 - \varepsilon_\infty\right)\sin\left(\delta\right), \tag{31}$$

and

$$\tan\delta = \frac{\varepsilon''}{\varepsilon'} = \frac{G_p}{i\omega C_p} \tag{32}$$

Note that $\tan\delta$ is independent of the geometric capacitance C_0. Equations (26) and (29) - (31) imply that

$$A^* = -i\omega C_0\varepsilon^* \tag{33}$$

so that

$$\sigma^* = kA^* = i\omega\mathrm{e}_0\varepsilon^*;\ \sigma' = \omega\mathrm{e}_0\varepsilon'';\ \sigma'' = \omega\mathrm{e}_0\varepsilon' \tag{34}$$

and

$$\rho^* = \frac{1}{\sigma^*} = \frac{1}{kA^*} = \frac{1}{i\omega\mathrm{e}_0\varepsilon^*};\ \ \rho' = \frac{\varepsilon''}{\mathrm{e}_0\omega\left(\varepsilon'^2 + \varepsilon''^2\right)}\ ;\ \rho'' = \frac{\varepsilon'}{\mathrm{e}_0\omega\left(\varepsilon'^2 + \varepsilon''^2\right)}. \tag{35}$$

The complex electric modulus, M^*, is defined as the reciprocal of ε^*:

$$M^* \equiv \frac{1}{\varepsilon^*}. \tag{36}$$

Thus

$$M^* = i\omega C_0 Z^* = \frac{i\omega C_0}{A^*} = i\omega \varepsilon_0 \rho^* = \frac{i\omega \varepsilon_0}{\sigma^*} \quad . \tag{37}$$

The dielectric loss ε'' is related to the optical absorption coefficient α(neper m^{-1}) by

$$\varepsilon''(\omega) = \frac{n'(\omega)\alpha(\omega)c}{\omega} \quad , \tag{38}$$

where n' is the real component of the complex refractive index and *c* is the speed of light in vacuo $(3.00\times10^8$ m/s$)$. The functions σ^*, ε^*, ρ^* and M^* are all analytical functions, whose components conform to the Cauchy-Riemann and Kronig-Kramers equations.

3.2 *Relaxation Times*

If an electric field across a dielectric sample is instantaneously decreased from E_0 to zero and kept there, the initially oriented dipoles will randomize over time and the polarization, *P*, and displacement, *D*, will decrease (recall that $D = \varepsilon_0 E + P$):

$$P_E(t) = P_E(0)\phi_E(t) \tag{39}$$

where $\phi_E(t)$ is the dielectric retardation function at constant *E*. The complex relative permittivity $\varepsilon^*(\omega)$ is related to the derivative of $\varepsilon(t)$ by

$$\varepsilon^* - \varepsilon_R = (\varepsilon_U - \varepsilon_R)\int_0^\infty -\left(\frac{d\phi_E}{dt}\right)\exp(-i\omega t)\,dt\,, \tag{40}$$

where ε_U and ε_R (both real [5]) are the limiting low and high frequency limits of ε', respectively. In the simplest case $\phi_E(t)$ is exponential:

$$\phi_E(t) = \exp\left(-\frac{t}{\tau_E}\right), \tag{41}$$

where τ_E is the dielectric retardation time at constant *E* [different from the relaxation time τ_D of eq. (22)]. Insertion of eq. (41) into eq. (40) yields the Debye equation [6]:

$$\varepsilon^* - \varepsilon_R = \frac{(\varepsilon_U - \varepsilon_R)}{1 + i\omega\tau_E}\,, \tag{42}$$

from which

$$\varepsilon' - \varepsilon_R = \frac{(\varepsilon_U - \varepsilon_R)}{1+\omega^2 \tau_E^2} \,, \tag{43}$$

$$\varepsilon'' = \frac{(\varepsilon_U - \varepsilon_R)\omega\tau_E}{1+\omega^2 \tau_E^2} = (\varepsilon_U - \varepsilon_R)\,\mathrm{sech}\left[\ln(\omega\tau_E)\right] \,, \tag{44}$$

$$\tan\delta \equiv \frac{\varepsilon''}{\varepsilon'} = \frac{(\varepsilon_U - \varepsilon_R)}{\varepsilon_U}\left[\frac{\omega\tau_E}{1+(\varepsilon_R/\varepsilon_U)\omega^2\tau_E^2}\right], \tag{45}$$

and

$$\sigma' = \mathrm{Re}(\mathrm{e}_0 \omega \varepsilon'') = \frac{(\varepsilon_U - \varepsilon_R)(\mathrm{e}_0/\tau_E)\omega^2\tau_E^2}{(1+\omega^2\tau_E^2)}. \tag{46}$$

Note that $\tan(\delta)$ has the same frequency dependence as ε'', but with a retardation time of $(\varepsilon_R/\varepsilon_R)^{1/2}\tau_E$ rather than τ_E. Equation (46) indicates that the conductivity increases from zero at low frequencies to a high frequency limit of

$$\sigma_R = (\varepsilon_U - \varepsilon_R)(\mathrm{e}_0/\tau_E). \tag{47}$$

3.3 *Distribution Functions*

If the retardation function is nonexponential, dielectric relaxation can be described in terms of a distribution of retardation times, $g(\ln\tau_E)$, defined by the relation

$$\phi_E(t) = \int_0^\infty g(\tau_E)\exp\left(-\frac{t}{\tau_E}\right)d\tau_E = \int_{-\infty}^\infty g(\ln\tau_E)\exp\left(-\frac{t}{\tau_E}\right)d\ln\tau_E. \tag{48}$$

Equation (42) then generalizes to

$$\varepsilon^* - \varepsilon_R = (\varepsilon_U - \varepsilon_R)\int_0^\infty \frac{g(\tau_E)}{1+i\,\omega\tau_E}d\tau_E = \int_{-\infty}^\infty \frac{g(\ln\tau_E)}{1+i\,\omega\tau_E}d\ln\tau_E \quad . \tag{49}$$

The distribution function can be characterized by its moments, given by

$$\langle\tau_E^n\rangle = \int_0^\infty \tau_E^n\, g(\tau)\,d\tau_E = \int_{-\infty}^{+\infty} \tau_E^n\, g\ln\tau\, d\ln\tau_E \tag{50}$$

for the n^{th} moment. The distribution function is normalized so that its zero$^{\text{th}}$ moment is unity. In terms of $\phi(t)$ the n^{th} moments are

$$\left\langle \tau_E^n \right\rangle = \left(\frac{1}{\Gamma(\omega)} \right) \int_0^\infty t^{n-1} \phi(t)\, dt \tag{51}$$

and

$$\left\langle \tau_E^{-n} \right\rangle = (-1)^n \left(\frac{d^n \phi_E}{dt^n} \right)\Bigg|_{t=0} \qquad \text{(integer } n > 1\text{)} \tag{52}$$

Dielectric relaxation produces a dispersion in the conductivity:

$$\begin{aligned} &\sigma_U = 0, \\ &\sigma_R = (\varepsilon_U - \varepsilon_R)\left\langle \frac{1}{\tau_E} \right\rangle. \end{aligned} \tag{53}$$

If a limiting low frequency conductivity σ_0 is present, this must be subtracted from the measured conductivity before the dielectric loss is calculated from eq.(31). If this is not done, the decrease in ε'' as $\omega \to 0$ predicted by eq. (44) will not occur, but will be masked by the rapid rise from the conductivity contribution

$$\varepsilon''_\sigma = \frac{\sigma_0}{\mathrm{e}_0 \omega} \tag{54}$$

It has been argued that this subtraction is physically meaningful only if the conductivity is unrelated to the dielectric loss process (as in aqueous solutions, for example). If the dielectric loss peak correlates with σ_0, as occurs in alkali silicate glasses [7-13] and most (all?) other ionic conductors, then the subtraction of σ_0 is artificial and other methods of data analysis are preferred (although this position is not universally accepted). This is the principle reason for not using the complex permittivity in analyzing highly conducting materials, and is the subject of section 4.

3.4 *Hamon Approximation*

Time and frequency domain data can be related by the approximate Hamon relation [14]

$$\varepsilon''(\omega) \approx (\varepsilon_U - \varepsilon_R)\left(-\frac{d\phi}{dt} \right)\left(\frac{5t}{\pi} \right);\ \omega t = 5\ , \tag{55}$$

derived from the approximation that the current is

$$i = \left(\frac{d\phi}{dt} \right) \sim t^{-n}. \tag{56}$$

No comparably simple relation exists between $\varepsilon'(\omega)$ and $\phi(t)$. Williams, Watts, Dev and North [15] have shown that for the decay function

$$\phi(t) = \exp\left[-\left(\frac{t}{\tau_0}\right)^{\beta}\right] \tag{57}$$

the Hamon approximation is accurate within 1% for $\omega\tau_0 > 1$, but fails for $\omega\tau_0 < 1$ and $\beta \geq 0.2$. For high frequencies, therefore, eq. (55) offers an acceptable approximation to the frequency domain Williams-Watts function, which cannot be expressed in terms of named functions.

3.5 *Equivalent Circuits*

The electrical response described by ε^* for an exponential decay function, the Debye relation eq. (42), is simulated by the equivalent circuit shown in Figure 1, in which the conductance G_p corresponds to the zero frequency conductivity and C_∞ to the limiting high frequency permittivity. Detailed discussions of the use of equivalent circuits are given in the literature [16], and we restrict ourselves here to noting that if, for a particular range of frequencies, the equivalent circuit of an experimental sample resembles that shown in Figure 1, then a dielectric loss will be observed in that frequency range. Generally speaking, a resistance and capacitance in series is often sufficient to produce dielectric loss behavior. An example of such a series circuit is electrode polarization, which at low frequencies can be approximated by a capacitance in series with the low frequency resistance of the sample. In this case a dielectric loss is observed with a retardation time given by the product of the polarization capacitance and sample resistance. Electrode polarization effects in solid electrolytes can often be a severe problem, and are discussed further in §4.3.

3.6 *Dielectric Relaxation in the Temperature Domain*

For many dielectric functions, ω and τ_E are interchangeable variables. Since τ_E varies with temperature, temperature can be used as an experimental variable to replace frequency. This is often done for experimental simplicity, and because changes in τ_E with temperature correspond to a much wider range in frequency than that of most audio and sub-audio frequency generators and detectors. The temperature dependence of τ_E often adheres to the Arrhenius relation

$$\tau_E = \tau_0 \exp\left(\frac{E_A}{RT}\right), \tag{58}$$

where τ_0 is independent of temperature, R is the ideal gas constant, and E_A is the activation energy. Then $\ln\tau_E = \ln\tau_0 + \frac{E_A}{RT}$ so that $\ln(\omega\tau_E)$ and E_A/RT are equivalent for a single

relaxation time dielectric. Equation (58) indicates that over the convenient temperature range from liquid nitrogen (77 K) to room temperature (300K), the retardation time can vary over a very large range. For an activation energy of 50 kJ/mol, for example, τ_E changes by a factor of 10^{25}, compared with 10^8 or so for conventional ac bridge techniques [Note added in 2013: this range is very much larger nowadays, nearer 10^{12}]. The temperature variable is therefore particularly useful for materials that have widely separated broad peaks, such as polymers. Temperature scans are difficult to analyze quantitatively, however, and it is difficult to evaluate the dispersion $(\varepsilon_U - \varepsilon_R)$ from temperature data because both ε_U, and to a less extent ε_R, are usually not well defined in the temperature domain. This dispersion can be approximated as [16]

$$(\varepsilon_U - \varepsilon_R) = \left(\frac{2}{R\pi}\right)\left\langle \frac{1}{E_A} \right\rangle^{-1} \int_0^\infty \varepsilon''(T)\, d(1/T) \ , \tag{59}$$

but this is approximate because of two assumptions that must be made for mathematical tractability: (a) $(\varepsilon_U - \varepsilon_R)$ is independent of temperature [16]; (b) $\langle E_A \rangle = 1/\langle 1/E_A \rangle$. The latter is an approximation because it can be shown from the Schmidt inequality that

$$\langle E_A \rangle \langle 1/E_A \rangle \geq 1, \tag{60}$$

and it is $\langle E_A \rangle$ that is obtained in the frequency - temperature domain ("transition map") rather than $\langle 1/E_A \rangle^{-1}$.

There are two situations where $\ln(\omega)$ and E_A/RT are not equivalent variables. First, there is not an equivalence for functions in which ω and τ_E are not invariably multiplied together (for example the conductivity of a Debye dielectric, eq. (46)). Second, they are not equivalent if the distribution of retardation times changes with temperature,

3.7 *Determination of Activation Energies*

The logarithm of the frequency $f_{\max}$, or the inverse temperature $1/T_{\max}$, at which ε'' passes through its maximum can be plotted against one another and the activation energy determined from the slope:

$$\langle E_A \rangle = R\left[\frac{d\ln(f_{\max})}{d(1/T_{\max})}\right] . \tag{61}$$

In some cases, however, the activation energy obtained in this way is ambiguous, depending on whether it is determined in the isothermal frequency domain or in the temperature domain at constant frequency. There is at least one explicit reference to this in the literature [17], where the frequency domain plot of $\ln f_{\max}$ vs. $1/T$ was found to be strongly curved whereas the plot

of $\ln f$ vs. $1/T_{max}$ was found to be linear. [Note added in 2013: this claim is suspicious but has not been examined by this author].

4. *CONDUCTIVITY RELAXATION*

4.1 *General Concepts and Basic Formalisms*

Relaxation of polarization induced by an electric field can occur in two physically distinct ways: dielectrically by rotation of dipoles or by trapped ions oscillating between sites, and by conductivity relaxation [18] arising from long range translational migration of point charges. The relaxation character of conductivity is demonstrated by the existence of a relaxation time, the Maxwell relaxation time defined in eq. (22). From the definitions $\varepsilon' = C_p/C_0$ and $\sigma_0 = e_0/C_0 R_p$ this Maxwell time is also given by

$$\tau_D = R_p C_p = \frac{e_0 \varepsilon_\infty}{\sigma_0} \quad . \tag{62}$$

This time is different from the "relaxation time" in the Fermi gas expression for electronic conductivity in metals, which is directly proportional to σ_0 [19]:

$$\tau_e = \left(m/ne^2\right)\sigma_0 \tag{63}$$

where n is the number density of charge carriers of effective mass m and charge e. The reason for the difference is that in the Fermi gas expression, τ_e is the time between electron scattering events (collisions with ions, other electrons, or phonons), whereas τ_D is the residence time between jumps to and from adjacent sites. Formally, the Maxwell conductivity relaxation time is a measure of the rate of decay of the polarization at constant displacement, i.e. the decay of the electric field E at constant D [18] (hence the subscript D). On the other hand, as noted already, the dielectric retardation time is a measure of the decay rate of the polarization at constant E, i.e. of D at constant E that has been referred to as τ_E. The two times are usually different, but are related by an expression to be discussed later [eq.(73)].

To analyze conductivity relaxation, it is helpful to describe it in terms of a function that exhibits the same sort of loss peak exhibited by ε'' for dielectric relaxation. The function ε'' itself is not suitable, because for a frequency invariant conductivity it exhibits a monotonic inverse proportionality to frequency [eq. (54)]. On the other hand, the two impedance functions, the electric modulus M^* [18] and complex resistivity ρ^* [20,21], are well suited for this purpose. The electric modulus was first defined by McCrum, Read and Williams [17], but its use in analyzing conductivity relaxation was first initiated and exploited by Macedo and coworkers [18].

The usefulness of M^* and ρ^* is illustrated by the simple system characterized by a frequency independent conductivity σ_0 and relative permittivity ε_∞ (the reason for the subscripts, which are superfluous here, will become clear when distribution functions are considered in section 5.2). The components of M^* are, in terms of the components of ε^*:

$$M' = \frac{\varepsilon'}{\varepsilon'^2 + \varepsilon''^2} \ , \tag{64}$$

$$M'' = \frac{\varepsilon''}{\varepsilon'^2 + \varepsilon''^2} . \tag{65}$$

Insertion of the relation between ε'' and σ_0 [eq. (54)] and between σ_0 and τ_D [eq. (62)] into these equations yields

$$M' = \left(\frac{1}{\varepsilon_\infty}\right)\frac{\omega^2 \tau_D^2}{1+\omega^2 \tau_D^2} \tag{66}$$

and

$$M'' = \left(\frac{1}{\varepsilon_\infty}\right)\frac{\omega\tau_D}{1+\omega^2 \tau_D^2}\left(\frac{1}{\varepsilon_\infty}\right)\mathrm{sech}\left[\ln\left(\omega\tau_D\right)\right] \ . \tag{67}$$

Equation (67) is identical in form to eq. (44) for ε'', so that M'' exhibits the desired peak, symmetric when plotted against $\ln(\omega)$. The components of ρ^* and M^* are related by

$$\begin{aligned} M' &= \omega \mathrm{e}_0 \rho'', \\ M'' &= \omega \mathrm{e}_0 \rho'. \end{aligned} \tag{68}$$

Thus, in analogy with eq. (67) for M'', ρ'' is given by

$$\rho'' = \left(\frac{1}{\mathrm{e}_0 \varepsilon_\infty \omega}\right)\frac{\omega^2 \tau_D^2}{1+\omega^2 \tau_D^2} = \rho_0 \frac{\omega\tau_D}{1+\omega^2 \tau_D^2} \ , \tag{69}$$

where

$$\rho_0 \equiv \frac{1}{\sigma_0} = \left(\frac{\tau_D}{\mathrm{e}_0 \varepsilon_\infty}\right) . \tag{70}$$

Equations (67) and (69) illustrate that M'' and ρ'' have the same frequency dependencies, but are weighted by ε_∞^{-1} and ρ_0, respectively. This is an important difference, that can be exploited to considerable advantage (*vide infra*).

For dielectric relaxations, M^* and ε^* are almost equivalent because a dielectric relaxation that exhibits a peak in ε'' will also exhibit a peak in M'' (although the shapes may differ). When ε' is significantly greater than ε'' (not uncommon) then approximately

$$M'' = \frac{\varepsilon''}{\varepsilon'^2 + \varepsilon''^2} \approx \frac{\varepsilon''}{\varepsilon'^2} = \frac{\tan\delta}{\varepsilon'}. \tag{71}$$

Insertion of eqs. (43) and (44) into eq. (65) for M'' yields [18,22]

$$M'' = \left(\varepsilon_\infty^{-1} + \varepsilon_0^{-1}\right)\left(\frac{\omega\tau_D}{1+\omega^2\tau_D^2}\right), \tag{72}$$

where [18,22]

$$\tau_D = \left(\frac{\varepsilon_\infty}{\varepsilon_0}\right)\tau_E. \tag{73}$$

Although it appears that a peak in M'' could be due to either a conductivity or dielectric process, and that M^* could not distinguish between them, this is not always so. If the relaxation is due to conductivity, the relaxation time τ_D, (or its average, see below) will be calculable from the limiting low frequency conductivity σ_0. An example of dielectric relaxation being correlated with σ_0 occurs in alkali silicate glasses and most (all?) other purely ionic conductors, that originally led to the inference that the dielectric loss is due to the same alkali migration process that produces σ_0 [7-13], and to which the modulus formalism and the concept of conductivity relaxation were first applied by Macedo and coworkers [18].

In the absence of electrode polarization, the low frequency behavior of M' is different for dielectric and conductivity relaxations. For dielectrics M' behaves as

$$\lim_{\omega\to 0} M' = \varepsilon_U^{-1}, \tag{74}$$

that contrasts with $\lim_{\omega\to 0} M' = 0$ for a conductivity relaxation [eq. (66)]. The last limit is conceptually important. The real part of the electric modulus is a measure of the restoring force in response to an electric field perturbation. This is finite for a dielectric relaxation, that can be interpreted as the charge storage ability (measured by ε_0) remaining finite as $\lim_{\omega\to 0}\varepsilon'' = 0$. For a conductivity relaxation the dielectric loss becomes infinite as $\omega \to 0$ and this dissipation completely overrides the storage capability. Thus no restoring force is observed and $\lim_{\omega\to 0} M' \to 0$, analogous to the mechanical modulus going to zero as the viscosity of a viscoelastic material dominates at low frequency and the elasticity disappears. Note added 2013: The non-zero limit eq. (74) is also observed for conductivity relaxations if there is electrode polarization that behaves as a series capacitance (*vide infra*).

4.2 *Distribution of Conductivity Relaxation Times.*

In direct analogy with eq. (49) for ε^*, M^* and ρ^* can also be described in terms of a distribution of relaxation times:

$$M^*(\omega) = M_\infty \int_0^\infty g(\tau)\frac{i\omega\tau}{1+i\omega\tau}d\tau = \int_{-\infty}^\infty g(\ln\tau)\frac{i\omega\tau}{1+i\omega\tau}d\ln\tau;$$

$$M'(\omega) = M_\infty \int_0^\infty g(\tau)\frac{\omega^2\tau^2}{1+\omega^2\tau^2}d\tau = M_\infty \int_{-\infty}^\infty g(\ln\tau)\frac{\omega^2\tau^2}{1+\omega^2\tau^2}d\ln\tau; \qquad (75)$$

$$M''(\omega) = M_\infty \int_0^\infty g(\tau)\frac{\omega\tau}{1+\omega^2\tau^2}d\tau = M_\infty \int_{-\infty}^\infty g(\ln\tau)\frac{\omega\tau}{1+\omega^2\tau^2}d\ln\tau.$$

where $M_\infty = 1/\varepsilon_\infty$. The expressions for ρ^* and its components are the same, except that the coefficient M_∞ is replaced by ρ_0. However, there is an important distinction between the effects of a distribution of conductivity relaxation times and a distribution of dielectric retardation times. It is easily shown [18] that

$$\sigma_0 = \lim_{\omega\to 0}(\sigma^*) = \frac{e_0\varepsilon_\infty}{\langle\tau_D\rangle} = \frac{e_0}{M_\infty\langle\tau_D\rangle}, \qquad (76)$$

$$\sigma_\infty = \lim_{\omega\to\infty}(\sigma^*) = e_0\varepsilon_\infty\left\langle\frac{1}{\tau_D}\right\rangle = \frac{e_0}{M_\infty}\left\langle\frac{1}{\tau_D}\right\rangle, \qquad (77)$$

$$\varepsilon_0 = \lim_{\omega\to 0}(\varepsilon^*) = \frac{\varepsilon_\infty\langle\tau_D^2\rangle}{\langle\tau_D\rangle^2} = \frac{\varepsilon_\infty e_0\langle\tau_D^2\rangle}{M_\infty\langle\tau_D\rangle^2}\ . \qquad ;. \qquad (78)$$

For conductivity relaxations, therefore, the dispersions in both conductivity and permittivity are determined by the breadth of the distribution function. This contrasts with dielectric relaxation, for which only the frequency range of the dispersion is affected by the distribution. The dependence of the dispersions in ε^* and σ^* on the distribution function can be interpreted as follows [18]. The permittivities of most materials generally vary by a factor of 10 or less, so that a distribution in relaxation times is determined primarily by the distribution of conductivities in the sample. Since polarization occurs at the interface of two regions of differing conductivity, a greater spread of conductivities will produce increased polarization. It is for this reason that the impedance formalisms M^* and ρ^* are particularly useful for analyzing interfacial polarization.

A distribution in retardation times for ε^* produces a dispersion in σ':

$$\sigma_U = 0,$$
$$\sigma_R = (\varepsilon_U - \varepsilon_R)e_0\langle 1/\tau_E\rangle. \qquad (79)$$

In modulus spectroscopy, a distribution of conductivity relaxation times cannot be distinguished in principle from dielectric and conductivity relaxations occurring together [18, 22]. However, if the average dielectric retardation time is much longer than the average conductivity relaxation time, $\langle\tau_E\rangle/\langle\tau_D\rangle \gg 1$, then the dielectric relaxation will not be seen because σ_0 will be much higher than the limiting high frequency dielectric loss conductivity σ_R:

$$\frac{\sigma_0}{\sigma_R} = \frac{\varepsilon_\infty}{(\varepsilon_U - \varepsilon_R)\langle\tau_D\rangle\langle 1/\tau_E\rangle} \quad \left(\to \infty \text{ for } \langle\tau_D\rangle/\langle\tau_E\rangle \approx \langle\tau_D\rangle\langle 1/\tau_E\rangle \to 0\right). \tag{80}$$

This phenomenon has been observed in systems for which the dielectric retardation time is essentially constant but whose conductivity is increased by addition of electrolyte [23,24]. These effects are ameliorated if conductivities can be measured with very high precision (see Schwann et al. [25], for example).

4.3 *Electrode Polarization*

The direct determination of the low frequency quantities ε_0 and σ_0 is often made difficult, and sometimes rendered impossible, by the effects of electrode polarization. For materials that are not electronic conductors, and for which charge transport across the electrode interface is not significant ("blocking electrodes"), polarization can be approximately simulated by a capacitance C_s in series with the sample [26, 27, 49]. Strictly speaking, a Faradaic impedance is in parallel with this, but for applied voltages that are below the decomposition potential of the sample, this can be neglected [27]. In this case it can be shown [18, 22] that the imaginary component of the electric modulus is unaffected provided C_s is much larger than the sample capacitance (often the case), and that only M' is affected at low frequencies:

$$\lim_{\omega\to 0}(M') = \frac{C_0}{C_s}. \tag{81}$$

This is a considerable advantage of the modulus formalism, since electrode polarization is a ubiquitous phenomenon. Electrode polarization also causes a rapid rise in ρ'' at low frequencies:

$$\lim_{\omega\to 0}(\rho'') = \frac{1}{\omega C_s}, \tag{82}$$

and is often characterized by two other low frequency effects: a rapid rise in ε' and, at lower frequencies, a decrease in σ'. It is these effects that prevent the observation of limiting low frequency values in ε' and σ'. The dispersion in ε' due to polarization generally occurs at much lower frequencies than the bulk conductivity dispersion:

$$\tau_{\text{electrode}} \approx \frac{e_0 C_s}{C_0 \sigma_0} \tag{83}$$

compared with

$$\tau_D \approx \frac{e_0 C_p}{C_0 \sigma_0}. \tag{84}$$

When $C_s \gg C_p$, then clearly $\tau_{electrode} \gg \tau_D$. However, the magnitude of the polarization dispersion (proportional to $\left(C_s - C_p\right) \approx C_s$) is correspondingly larger, so that the high frequency tail of the polarization dispersion extends well into the bulk relaxation region.

The phenomenon is best illustrated by a specific example. Consider a system where the low frequency bulk capacitance $C_p \approx 10^{-11}$ F (10 pF), the electrode capacitance $C_s \approx 10^{-8}$ F $\left(10^4 \text{ pF}\right)$, and the bulk resistance R_p is 10^7 ohm. The bulk dispersion is therefore centered at ca. $\omega \approx 1/\left(R_p C_p\right) \approx 10^4$ rad sec^{-1}, and the polarization is centered at $\omega = R_p C_s = 0.1$ rad/sec. For a typically broad bulk distribution function the low frequency plateau of ε' will occur at about $\omega \approx 10^2$ rad sec^{-1}, at which frequency the polarization gives a capacitance of $\approx \left(\omega^2 R_p^2 C_s\right)^{-1} \approx 10^{-10}$ F (100 pF), an order of magnitude higher than the bulk capacitance. On the other hand, the low frequency dispersion in conductivity due to polarization has barely begun at $\omega \approx 10^2$ rad sec^{-1} (the decrease in conductivity is about 1%):

$$\frac{\sigma_{\text{electrode}}}{\sigma_0} \approx \frac{\omega^2 \tau_{\text{electrode}}^2}{1 + \omega^2 \tau_{\text{electrode}}^2} \approx 0.99 \text{ for } \omega \tau_{\text{electrode}} \approx 10. \tag{85}$$

Note that since $\tau_{\text{electrode}}$ is determined by $C_s \cdot R_p$, the high frequency conductivity for the electrode polarization dispersion is σ_0 itself [eq. (47)]:

$$\sigma_\infty \left(\text{electrode}\right) = \frac{\left(\varepsilon_0 - \varepsilon_\infty\right) e_0}{\tau_E} = \frac{\left(\varepsilon_0 - \varepsilon_\infty\right) e_0 \varepsilon_\infty}{\tau_D \varepsilon_0} = \frac{\left(\varepsilon_0 - \varepsilon_\infty\right) \sigma_0}{\varepsilon_0} = \left(\frac{C_s - C_p}{C_s}\right) \sigma_0 \approx \sigma_0 \tag{86}$$

for $C_s \gg C_p$. Effects similar to electrode polarization can arise from other causes as well. One is poor contact between the electrode and the sample, that can result in a capacitance due to air gaps being in parallel with a conductance at the contact points. For example, air gaps and poor electrode contacts in general have been shown to give rise to spurious dielectric losses in undoped alkali halides [28] and is suspected to be responsible for the poor reproducibility of many reported dielectric losses in the alkali halides.[29]. Space charge effects can also give rise to a capacitance at the electrode [30] although it is generally smaller than a typical double layer capacitance.

If the applied voltage is too high then electrolysis can occur and a Faradaic impedance appears in parallel with the double layer capacitance. The Faradaic impedance is usually taken

to be a (voltage dependent) resistance due to electron transfer, that is voltage dependent, in series with the Warburg impedance [31] due to diffusion of the electrolysis products. The latter has a frequency dependence given by

$$\rho_W^* = \frac{(1-i)\,k_W}{\omega^{1/2}}, \tag{87}$$

where k_W is a function of electrode product concentration and the diffusion coefficient [32]. The other functions for the Warburg impedance are

$$\sigma_W^* = \left(\frac{1}{2k_W}\right)(1+i)\,\omega^{1/2}, \tag{88}$$

$$\varepsilon_W^* = \left(\frac{1}{2\mathrm{e}_0 k_W}\right)(1+i)\,\omega^{-1/2}, \tag{89}$$

$$M_W^* = \sigma_W^* = \mathrm{e}_0 k_W\,(1-i)\,\omega^{1/2}. \tag{90}$$

The Warburg impedance can occur only when the concentration of mobile ions adjacent to the electrode is independent of the potential difference between the electrode and electrolyte and is therefore unlikely if there is only one mobile species present, as occurs in most solid electrolytes. However, Bruinink and Broers [34] observed a Warburg like impedance in parallel with the bulk impedance in KHF_2, and attributed it to heterogeneities within the electrolyte. The effect was observed over a small range in frequency (a factor of 220). Consistent with this, Armstrong et al.[20] found it difficult to distinguish between a Warburg impedance and a rough electrode surface.

In complex plane plots of all four basic functions the Warburg impedance gives a straight line of slope +1, since the real and imaginary components of all four functions have the same frequency dependence. The same occurs for any function which has a simple power frequency dependence, $\omega^{\pm\alpha}$, since it can be shown from the Kronig-Kramer relations [eqs. (14) , (15)] that if one component of a complex function has such a frequency dependence then the other component has the same dependence. Also, the corresponding time domain functions can be shown to be proportional to $t^{\mp\alpha}$. A straight line in the complex plane does not necessarily indicate, however, that an electrode or other interfacial phenomenon is occurring. In fact, Jonscher [35] observes that such behavior is a common dielectric response shared by a large variety of materials, particularly at high frequencies, and has given a theoretical account of it [36] that has been generalized [37].

The effects of a Warburg impedance in several circuit configurations have been described by Bauerle [38] in the complex admittance plane. In the complex impedance plane, a Warburg impedance in series with the bulk electrolyte gives a low frequency spike oriented at $\pi/4$ to the real axis, analogous to the vertical spike of a pure capacitance (see section 4.3.1). If a capacitance and Warburg element are in parallel and of comparable magnitude, the spike will make an angle between $\pi/4$ and $\pi/2$ with the real axis, and is therefore indistinguishable from

the behavior of a rough electrode [38]. However, provided no large amount of curvature is present the same extrapolation procedure for obtaining the bulk resistance in the presence of a purely capacitive electrode impedance can be used (§4.5.1).

4.4. *Illustration of Electrode Polarization and Bulk Relaxations in the Frequency Domain.*

The relations given in the previous 3 subsections are now illustrated using an idealized system consisting of the simple equivalent circuit shown in Fig. 2a, and a geometric cell constant of 1.0 cm^{-1} = 100 m^{-1}. The distribution function for this circuit consists of two single relaxation times $\tau_1 = \left(10^8\ \Omega\right)\cdot\left(10^{-12}\ \mathrm{F}\right) = 10^{-4}$ s and $\tau_2 = \left(10^6\ \Omega\right)\cdot\left(10^{-12}\ \mathrm{F}\right) = 10^{-6}$ sec, corresponding to the two parallel *RC* elements. Electrode polarization is simulated by the capacitance C_s in series with them. Such a circuit successfully simulates the electric response of a variety of polycrystalline electrolytes, including an electronically semiconductor [40], a superionic conductor [20], and an average ionic conductor [41]. Generally speaking, one of the *RC* elements simulates a crystal impedance and the other *RC* element simulates any inter-granular impedance.

The relaxation time averages appearing in eqs. (76)- (78) are

$$\begin{aligned}
\left\langle \tau_D \right\rangle &= \frac{\left(\tau_1 + \tau_2\right)}{2} = 5.05\times10^{-5}\ \text{sec};\\
\left\langle \tau_D^2 \right\rangle &= \frac{\left(\tau_1^2 + \tau_2^2\right)}{2} = 5.0005\times10^{-9}\ \text{sec}^2;\\
\left\langle \tau_D^{-1} \right\rangle &= \frac{\left(\tau_1^{-1} + \tau_2^{-1}\right)}{2} = 5.05\times10^{+5}\ \text{sec}^{-1}.
\end{aligned} \tag{91}$$

The high frequency permittivity is

$$\varepsilon_\infty = \frac{C_{circuit}C_s}{C_0\left(C_{circuit}+C_s\right)} = \frac{\left(0.5\times10^{-12}\ \mathrm{F}\right)\left(10^{-6}\ \mathrm{F}\right)}{\left(8.854\times10^{-14}\ \mathrm{F}\right)\left(10^{-6}\ \mathrm{F}\right)} = 5.647, \tag{92}$$

and from eq. (78)

$$\varepsilon_0 = \varepsilon_\infty\left(\frac{\left\langle \tau_D^2 \right\rangle}{\left\langle \tau_D \right\rangle^2}\right) = \left(5.647\right)\frac{\left(5.0005\times10^{-9}\right)}{\left(5.05\times10^{-5}\right)^2} = 11.07. \tag{93}$$

From eqs. (76) and (77) for σ_0 and σ_∞:

$$\sigma_0 = \frac{\mathrm{e}_0\varepsilon_\infty}{\left\langle \tau_D \right\rangle} = \frac{\left(8.854\times10^{-12}\ \mathrm{F/m}\right)\left(5.647\right)}{5.05\times10^{-5}\ \text{sec}} = 9.901\times10^{-9}\ \mathrm{S/m}; \tag{94}$$

$$\sigma_\infty = \mathrm{e}_0 \varepsilon_\infty \left\langle \tau_D^{-1} \right\rangle = \left(8.854\times10^{-12}\ \mathrm{F/m}\right)\left(5.647\right)\left(5.05\times10^{+5}\ \mathrm{sec}\right)$$
$$= 2.525\times10^{-7}\ \mathrm{S/m}. \qquad (95)$$

The frequency dependences of σ^* and ε^* are given in Figs. 2b and 2c, and those of ρ^* and M^* are given in Figs. 2d and 2e. The corresponding complex plane plots are given in Figs. 3a-3d. Several features in these figures illustrate many of the observations made in previous sections:

(1) The relative heights of the loss modulus and resistivity peaks are different. This reflects the different weighting of the two functions [eqs. (67), (69)], since $1/\varepsilon_\infty = C_0/C_p$ and $\rho_0 = R_p/k = R_p C_o/\mathrm{e}_0$. For the component circuit elements shown in Fig. 2a the two C_p values are the same and the two peaks in *M"* are equal in height. However the resistances differ and the lower resistance (higher frequency) relaxation gives a smaller peak in $\rho"$, which on the linear scale of Fig. 2d is not evident (see inset for logarithmic scale). If the parallel *RC* elements differed in capacitance instead, the two modulus peaks would differ in height with the higher capacitance (lower frequency) relaxation being suppressed. This is discussed in detail in the literature [4], and as will be shown in the §5.32, it is of considerable help in analyzing systems that contain high capacitance effects, such as are commonly encountered in systems containing thin interfaces (e.g. intergranular impedances in polycrystalline solid electrolytes).

(2) After subtraction of the limiting low frequency conductivity contribution $\sigma_0/\mathrm{e}_0\omega$ from the dielectric loss $\varepsilon"$, and the infinite frequency permittivity contribution $\mathrm{e}_0\omega\varepsilon_\infty$ from the imaginary conductivity component $\sigma"$, both $\varepsilon"$ and $\sigma"$ exhibit a single peak that lies between the modulus and resistivity peaks. This occurs because at intermediate frequencies the high frequency relaxation element behaves as a pure resistance and the low frequency relaxation element as a pure capacitance, and as discussed above (§3.5) this series combination gives a peak in the admittance formalisms.

(3) The decrease in conductivity and increase in permittivity at low frequencies is due to the series capacitance. This simulated electrode polarization causes the low frequency rise in $\rho"$ [eq.(35)]. In the equivalent circuit the value of this capacitance was chosen to ensure a clean separation between the simulated polarization effects and the bulk relaxations, but as will be demonstrated in §5.3.2 considerable overlap occurs in typical experimental situations.

(4) The complex plane plots shown in Figs. 3, although qualitatively useful, are less informative than the spectra shown in Figs. 2. For example, it is impossible to compare the relative frequencies of the maxima in *M"* and $\rho"$ because frequency is absent from complex plane plots. Nonetheless, complex plane plots are sometimes advantageous. For example, the complex resistivity plane is useful for estimating σ_0 in the presence of severe polarization [20] (see section 4.3.1). The spike in the resistivity plane (Fig. 3c) is due to the simulated electrode polarization and occurs because each *RC* relaxation shows up in the complex plane as a semicircle with radius *R*, and the pure series capacitance has an infinite resistance and radius. The zero frequency conductivity also shows up as a spike in the complex permittivity plane, corresponding to the infinite conductivity dielectric loss at zero frequency, eq. (54).

(5) The increase in conductivity above its limiting low frequency value occurs at a frequency that closely corresponds to the inverse average relaxation time (arrowed Fig. 2b). This is often observed in experimental data as well, and in cases where the plateau is well

defined it is then possible to determine if the rise is due to a conductivity relaxation. If it is, then the angular frequency at which the rise occurs is related to the plateau conductivity σ_0 by the relation

$$\omega \approx \frac{\sigma_0}{e_0 \varepsilon_\infty}, \tag{96}$$

obtained by putting $\omega\tau_D \approx 1$. In the absence of specific data ε_∞ may be approximated to be 7 in this expression.

4.5 *Determination of Zero Frequency Conductivity from AC Data.*

Because of polarization and other effects such as those due to intergranular impedances in polycrystalline preparations, the limiting low frequency conductivity σ_0 seen in Fig. 2b is not observed in some experimental data. However, there are several methods that can be used to make a reasonable estimate of σ_0, and these are discussed here. Before this is done, however, the importance of a correct determination of σ_0 and some of the spurious effects resulting from an incorrect determination are illustrated.

If $\ln\sigma$, taken at a fixed frequency, is plotted as a function of $1/T$ in the usual Arrhenius plot, breaks in the curve can result from polarization and bulk relaxation effects. If the measuring frequency lies in the range within which polarization is important at a particular temperature, then the measured conductivity is lower than σ_0 by an amount that increases with increasing temperature because of the shift to higher frequencies of the polarization phenomenon. This results in a spuriously low observed activation energy at high temperatures. Similarly, if the measuring frequency lies in the bulk relaxation range the measured conductivity exceeds σ_0 by an amount which decreases with increasing temperature. This also results in a spuriously low apparent activation energy, but in this case the deviation occurs at low temperatures. Both these phenomena are illustrated in Fig. 4.

When the high frequency conductivity is proportional to frequency raised to a power near unity, such as occurs in electronic amorphous semiconductors [42], the fixed frequency conductivity will become nearly independent of temperature at low temperatures. This was observed by Le Cleach and Palmier [43] for example, and occurs because a change in temperature that increases the conductivity by an order of magnitude at all frequencies also shifts the conductivity spectrum to higher frequencies by about an order of magnitude, thus moving a lower frequency-lower conductivity point up to the measuring frequency.

An accurate determination of σ_0 is required if relaxation data are analyzed in terms of the complex permittivity, where σ_0 must be subtracted before data processing is done. This has been noted above, and the difficulties that this subtraction causes have been discussed by Ravaine and Souquet [44].

4.5.1 *Use of the Complex Resistivity Plane*

The complex resistivity plane (or the complex impedance plane) has been used extensively by Armstrong et al. [41] for determining σ_0 in the presence of severe polarization. The principle of the method is to extrapolate the polarization spike (as in Fig. 3c, for example) to the ρ' axis, and to equate $\rho_0 = 1/\sigma_0$ with the intercept. In many cases the spike occurs at an angle with the ρ' axis that has been attributed to surface roughness at the electrode interface [38]. Curvature of the spike is also sometimes observed. As mentioned in §4.3, this would be expected if the Faradaic impedance that is in parallel with the capacitance has a significant resistive component at the measuring frequency and voltage.

The complex resistivity plane has also been used by Ravaine and Souquet [44] for obtaining σ_0 for alkali silicate glasses in the presence of mild electrode polarization. In this case the high frequency complex resistivity spectrum is fitted to the Cole-Cole function (see Appendix A2.3), and the low frequency conductivity is determined by extrapolation of the semicircle in the complex plane.

4.5.2 *Modulus and Resistivity Spectra*

In cases where polarization and bulk relaxation effects overlap to the extent that no plateau in σ' is observed, σ_0 can be calculated from eq. (76) if $\langle \tau_D \rangle$ and ε_∞ are known. The latter two quantities can be estimated by fitting M'' to some empirical function and calculating $\langle \tau_D \rangle$ and ε_∞ from best fit parameters. As explained in §3.3, M'' suppresses high capacitance effects such as those due to polarization so that only the bulk relaxation is included in the fitted function. This is demonstrated in detail in §4.1.

The maximum value of ρ'', $\rho''_{\max}$, can also be used to estimate σ_0. If the half width of the peak in ρ'' is Δ decades (e.g. 1.14 for a Debye curve), the value of σ_0 is given to within about ±10% by

$$\sigma_0 = \frac{1}{1.75\,\Delta\rho''_{\max}}. \tag{97}$$

If only one side of a peak is observed, it is still possible to estimate σ_0 by assuming the peak in ρ'' to be symmetric. With the same assumption of symmetry σ_0 can also be estimated from the value of ρ' at the angular frequency $\omega_{\max}$ of maximum ρ'':

$$\sigma_0 \approx \frac{1}{2\rho'(\omega_{\max})}. \tag{98}$$

Both of these methods are essentially the spectral equivalents of the complex resistivity plane method used by Ravaine and Souquet [44] (§4.5.1).

5. *Applications of AC Formalisms to Experimental Data.*

It is an unfortunate fact that the frequency dependences of σ' and ε' are rarely both reported together in the literature as a function of frequency. In those cases where both are given the data are almost invariably displayed graphically, so that it is difficult to obtain accurate data from most publications for further processing. For these reasons most of the examples in this section are from the author's own work, although many of the details are given here for the first time.

5.1 *Applications of the Complex Admittance Formalism to Polycrystalline Electrolytes and Electrode Phenomena.*

One of the first uses of complex plane plots was in the analysis of polycrystalline yttria-zirconia electrolytes by Bauerle [38]. He gives an extensive discussion of equivalent circuits and their corresponding complex admittance plane plots. We restrict our attention here to the equivalent circuit used by Bauerle in the analysis of his data, shown in Fig. 5a. The complex admittance plane plot for this circuit is given in Fig. 5b. In the equivalent circuit one of the parallel elements (R_1C_1) represents the electrode interface, the capacitance being due essentially to a double layer and the resistance of an oxygen-gas – oxide ion charge transfer process [37]. The other element (R_2C_2) represents grain boundary ("constriction" [37]) impedances, and the series resistance R_3 is the sample resistance. The experimentally observed complex admittance plane plots (Fig. 5c) were in excellent agreement with the equivalent circuit's predicted admittance plane behavior. Furthermore the zero frequency conductivity predicted from the complex plane plot was in excellent agreement with separate 4-terminal conductance data [37], and the expected dependence of the electrode impedance on such things as oxygen partial pressure was observed.

For a system as complex as this, this is an impressive correlation. However, the method has several disadvantages. First, in assuming that the bulk material acts as a pure resistance the analysis automatically assumes that the measuring frequencies are well below the conductivity relaxation frequency. This can, in general, only be confirmed retrospectively by demonstrating that the derived value of R_3 is sufficiently low. Second, if one places a capacitance in parallel with R_3 due to the bulk material then there are three relaxing elements in the circuit. The complex admittance, however, exhibits only two semicircles which reflect the *differences* between the relaxing elements. Third, if the observed relaxations overlap an assumption has to be made about the shapes of the two relaxations before extrapolations can be made. For example, it might have to be assumed that both relaxations are described by the Cole-Cole function, with the centers of the complex plane semicircles lying below the real axis. This was the case for Bauerle's data and an accurate analysis was accomplished, but this would not be expected to occur in general.

On the other hand, spectra of the electric loss modulus M'' and resistivity ρ'' would, in principle, exhibit three peaks corresponding to the three relaxations, from which the values of each R and C could be determined directly if overlap was not too great and the frequency range was sufficiently large. A detailed comparison of the relative merits of this method over complex admittance and complex permittivity methods has been given in §4.5.

5.2. *Conductivity Relaxations in Homogeneous Materials.*

5.2.1. *Analysis of Conductivity Relaxation in Glasses Using the Modulus and Resistivity Formalisms.*

Applications of the complex modulus and complex impedance formalisms are illustrated here using data of Hodge and Angell [45] on glassy aqueous acids. Although these electrolytes are rather unusual chemically their conductivity relaxation behavior is very similar to that of glassy conductors such as the alkali silicates [45].

The frequency dependencies of σ', ε' and M'' for one of the glasses are shown in Fig. 6a. The spectrum of ρ'' and the complex plane plot of ρ'' vs ρ' are shown in Figs 6b and 6c respectively. Features of interest are the absence of plateaus in σ' and ε' at low frequencies, and the continuous increase in σ' with increasing frequency. The solid lines are derived from the best fit Davidson-Cole function for the electric loss modulus M'', as discussed below.

The loss modulus spectrum is characterized by a long high frequency tail that is approximately described by the Davidson-Cole function (solid line in Fig 6a**).** For the purpose of illustration, the technique for fitting this particular function was as follows. The peak height, $M''_{\max}$, and width at half height (Δ), were determined to about ±2%. The Davidson-Cole parameters γ (that determines Δ) and M_∞ (that together with Δ determines $M''_{\max}$) were calculated from the expressions given in Appendix A2.1. For a spectrum as wide as that observed here the value of Δ, and more especially γ, is sensitive to the value $M''_{\max}$. Thus, great care is needed to ensure an accurate determination of the latter. The value of the Davidson-Cole parameter τ_0 is determined by the frequency, $f_{\max}$, at which $M''_{\max}$ occurs, or the upper frequency $f^+_{1/2}$ at which the spectrum falls to $M''_{\max}/2$. In this case there is considerable uncertainty in $f_{\max}$ because of the widely spaced frequency intervals (the reason for which is given in the original paper). However, τ_0 can be accurately determined from the two frequencies at which the spectrum attains a value of $M''_{\max}/2$, particularly by $f^+_{1/2}$, from the expressions given in Appendix A2.2.

The Davidson-Cole parameters could not be obtained from the high frequency data in complex plane plots [46] because the high frequency data lay above the Davidson-Cole prediction, thus invalidating the complex plane relations.

The frequency dependencies of σ' and ε' were calculated from the Davidson-Cole function for M'' and M':

$$\sigma' = \mathrm{e}_0\,\omega\varepsilon'' = \mathrm{e}_0\,\omega\left(\frac{M''}{M'^2 + M''^2}\right),$$
$$\varepsilon' = \mathrm{e}_0\,\omega\left(\frac{M'}{M'^2 + M''^2}\right). \qquad (99)$$

The values of σ_0, ε_0 and ε_∞ were also obtained from the Davidson-Cole parameters (see Appendix A2.1 for relevant equations):

$$\sigma_0 = \frac{\mathrm{e}_0}{M_\infty \langle \tau_D \rangle} = \frac{\mathrm{e}_0}{M_\infty \gamma \tau_0} = 2.39\times10^{-7}\ \mathrm{S/m}; \qquad (100)$$

$$\varepsilon_\infty = 1/M_\infty = 9.52\,; \tag{101}$$

$$\varepsilon_0 = \varepsilon_\infty \left[\frac{\tau_D^2}{\langle \tau_D \rangle^2} \right] = \varepsilon_\infty \left(\frac{1+\gamma}{2\gamma} \right) = 19.1\,. \tag{102}$$

The Davidson-Cole σ' and ε' spectra, calculated from eq. (99), are shown as solid lines in Fig. 6a. They clearly illustrate the suppression by the modulus formalism of the low frequency high capacitance polarization relaxation.

The calculated value of σ_0 is close to the inflection point of the conductivity spectrum. This occurs quite frequently, judging from published data. The inverse average relaxation time $1/\langle \tau \rangle$ is also close to the radial frequency at which departures from the (calculated) plateau value of σ begin to be significant, indicating that the dispersion in σ is due primarily to a conductivity relaxation (eq. (76)). The deviations at high frequencies are due to the experimental values of M'' exceeding the Davidson-Cole fit. As discussed elsewhere [24, 45], this might be caused by a higher frequency dielectric relaxation process or a resonance absorption.

The resistivity spectrum is shown in Fig. 6b. The severe polarization evident in the σ' and ε' data is also reflected in the ρ'' spectrum. In fact, the effect is so severe that it is impossible to extract useful information from the ρ'' spectrum. The complex resistivity plane is also of limited use (Fig. 6c). If the polarization "spike" is extrapolated to the ρ' axis, a value for σ_0 of 3.2×10^{-7} S/m is obtained, but comparison with the σ' spectrum indicates that this is quite unreasonable. The reason for the failure in this case is that the data do not extent to low enough frequencies. The polarization is also too close to the bulk relaxation for the method of Ravaine and Souquet [44] to be used. However, for the purposes of illustrating the latter method, the ρ'' spectrum is calculated from the Davidson-Cole fit to the modulus spectrum and is shown as the solid curve in Fig. 6b.

The calculated ρ'' spectrum is well fit by the Cole-Cole function [47]. However, it must be pointed out if ρ^* conforms exactly to a Cole-Cole function then the modulus spectrum has pathological properties, e.g. $\lim_{\omega\to\infty}(M'') \to \infty$ [78]. The Cole-Cole function for ρ' is

$$\rho' = \frac{\rho_0 \left[\sin(\alpha\pi/2) + (\omega\tau_0)^{\alpha-1} \right]}{\left[2\sin(\alpha\pi/2) + (\omega\tau_0)^{1-\alpha} + (\omega\tau_0)^{\alpha-1} \right]}\,. \tag{103}$$

As $\omega \to 0$, this becomes (since $0 < \alpha \le 1$)

$$\lim_{\omega\to 0} \left[\sin(\alpha\pi/2) \right] (\omega\tau_0)^{\alpha-1} \to \infty\,. \tag{104}$$

Also

$$\lim_{\omega\to\infty}\left(M''\right)=\lim_{\omega\to\infty}\left(\mathrm{e}_0\,\omega\rho'\right)=\lim_{\omega\to\infty}\left[\mathrm{e}_0\,\omega\rho_0\sin\left(\alpha\pi/2\right)\left(\omega\tau_0\right)^{\alpha}/\tau_0\right]\to\infty. \qquad (105)$$

Thus the Cole-Cole function is unphysical when applied to resistivity data. However, there is evidently another function that is very similar to the Cole-Cole distribution that does not have these pathological consequences. The data suggest quite strongly, for example, that a Davidson-Cole distribution in M^* is almost equivalent to a Cole-Cole distribution in ρ^* (see Figure A2.2).

It is possible that the resistivity spectrum predicted from the Davidson-Cole function for M^* is inappropriate in this case, for example because some bulk relaxation information is being suppressed by M^* which might contribute to ρ^*. However, Ravaine and Souquet [12, 44] found that the ρ^* data for alkali silicate glasses were well fit by the Cole-Cole function, and it has been demonstrated by Hodge and Angell that the Davidson-Cole function also provides good fits to M^* data for alkali silicate glasses. Thus, for the purposes of discussion and illustration, we shall assume that the calculated derived ρ'' spectrum reflects the full bulk relaxation spectrum.

The expression for estimating σ_0 from the ρ'' spectrum (eq. 97), is illustrated by this example. Of course, since the M'' spectrum from which ρ'' is derived also gives the correct σ_0, it can be said quite correctly that this is simply demonstrating self consistency. However, eq. (97) is independent of the distribution function for ρ^*, and it is appropriate to test it in this case. The half-width of the derived ρ'' spectrum is 1.25 decades, and its maximum is 1.9×10^{6} Ω.m. When inserted into eq. (97) these values give an estimate for σ_0 of 2.4×10^{-7} S/m, compared with 2.37×10^{-7} S/m from the modulus spectrum. Extrapolation of the Cole-Cole arc in the complex resistivity plane (Fig. 6c) gives a value for σ_0 of 2.4×10^{-7} S/m.

Thus although electrode polarization in this particular set of data is severe, its effects can be usefully suppressed by the M^* formalism. The nature of the polarization process, e.g. to what extent it can be simulated by a pure capacitance, is best studied with the ρ^* formalism. The two formalisms are therefore complementary, and enable different features of the total relaxation spectrum to be projected at will.

5.2.2. *Conductivity Relaxation in Single Crystal Beta Alumina.*

Spectra of M'' and ρ'' for single crystal beta alumina at −160°C were measured and analyzed by Grant and Ingram [48,60]. They calculated the modulus spectra of single crystal β-alumina in orientations perpendicular and parallel to the conductance plane, the impedance spectrum for the parallel orientation, and the dielectric loss spectrum for the perpendicular direction. These spectra are shown in Fig. 7, from which it is apparent that the impedance peaks in the parallel orientation occur at about the same frequency as the modulus and dielectric loss spectra in the perpendicular orientation.

The activation energy of the parallel impedance spectrum (18.4 kJ mole^{-1}) was comparable with that of the perpendicular dielectric loss spectrum (16.2 kJ mole^{-1}). The authors suggested that in the perpendicular orientation sodium beta alumina was a classic Maxwell layered dielectric [64] with the spinel blocks acting as the dielectric layers and the conduction planes acting as the conductors. The activation energy for the dielectric loss is thus

determined by the conductivity of the conducting layers, which the data suggest is similar in directions parallel and perpendicular to the conduction planes.

The enormous width of the modulus spectrum for single crystal sodium beta alumina in the parallel orientation [60, 61] is suggestive of a very wide distribution of relaxation times. The impedance and modulus spectra together suggest that this width may be due to a bimodal distribution function. Grant and Ingram suggested that, for the low temperature at which their data were taken, the low frequency conductivity is determined by an activated localized ion motion that is either the same in both orientations or is perpendicular to the conduction plane. The higher frequency conductivity relaxation, that contributes to the modulus spectrum but not to the impedance spectrum, results from a relatively free motion of the activated ions that is characterized by a low activation energy. It therefore appears that these workers have achieved a remarkable experimental separation of the "rattle and jump" components of the classical conductivity mechanism. Although not mentioned by the authors, this mechanism is also consistent with the low temperature localization of sodium ions deduced from nmr measurements [66]. At higher temperatures, the localized activation is not the rate determining step and the well known low activation energy for conductivity in sodium beta-alumina results.

This work is an excellent demonstration of the fine detail which can be deduced from experimental data if the correct formalisms are used. The speculations discussed above could not have been made with the raw conductivity and permittivity data alone.

5.3 *Analysis of Interfacial Relaxations*

5.3.1 *Electrode Effects*

It is assumed in the following discussion that the applied voltage is below the lowest decomposition potential for the electrode and electrolyte being studied. Thus the electric response characteristics of electrochemical reactions at the electrode will not be considered here; a review for aqueous solutions has been published [49].

Generally speaking, electrode polarization is characterized by a high capacitance in series with the bulk sample. The series circuit indicates that an analysis in terms of impedance formalisms such as the complex electric modulus or complex resistivity is preferable to that of admittance formalisms such as the complex permittivity or conductivity. Since the electric modulus formalism suppresses high capacitance phenomena it is the complex impedance or complex resistivity that is more generally useful. If electrode polarization is a problem only at the low frequency end of an experimentally accessible range then it can be suppressed by using the electric modulus formalism. However, if polarization dominates most of the accessible frequency range and it is desired to make high frequency extrapolations to obtain data relating to the bulk sample then the complex impedance plane or impedance spectra are better used. This section is devoted primarily to such methods of extrapolation.

5.3.1 (i) *Complex Impedance Plane Analysis of Electrode Polarization in Sintered β" Alumina.*

The use of the complex plane in extrapolating polarization phenomena to get bulk data has been used extensively by Armstrong and coworkers in their studies of superionic conductors such as sodium beta alumina [38, 41] and silver rubidium iodide [20, 50-53], and some illustrative examples taken from their work are shown in Fig. 8. A pure (not leaky) capacitance at the electrode interface gives a vertical spike in the complex impedance plane

(see sections 3.3-3.5 and Fig. 3c), but for these data the spike occurs at an acute angle to the real axis in one case (Fig. 8a), is curved in the other (Fig. 8b).

The sloping straight lines were ascribed to surface roughness at the electrode [38]. Curvature of the spikes might also result from a Warburg impedance [20] and/or a Faradaic charge transfer resistance in parallel with the polarization capacitance. As seen in Fig. 8b, however, the curvature is small and reasonable extrapolations can still be made.

Also illustrated in Fig. 8b is the case where the polarization spike overlaps significantly with the semicircle associated with a parallel *RC* element (usually corresponding to the bulk impedance, including intergranular effects in polycrystalline solid electrolytes). Note that although the different surface preparations significantly affect the overall impedance spectra, all of the extrapolations give the same value of σ_0. Electrode polarization also manifests itself as a rapidly rising low frequency increase in Z'' and ρ''.

5.3.1 (ii) *Complex Impedance Plane Analysis of Atmosphere Dependent Electrode Effects in* $\alpha-$ *and* $\beta-$ KHF_2.

Another example of complex impedance plane analysis is found in the study of both phases of KHF_2 by Bruinink and Broers. In an atmosphere of hydrogen with platinum paint electrodes, the complex plane plot of data for $\alpha-KHF_2$ was consistent with a Warburg impedance (§4.3) in parallel with the bulk resistance and capacitance [54], and extrapolation to the real Z' axis gave a value of σ_0 in agreement with the separately determined d.c. value. This is shown in Fig. 9a. The plot shows no indication of interfacial polarization, consistent with $\alpha-KHF_2$ being a proton conductor and the platinum paint electrodes being ideally reversible hydrogen electrodes with no polarization. This contrasts with the low frequency behavior of a $\alpha-KHF_2$ in a vacuum, shown in Fig. 9b. Here a double layer capacitance of ca. 44 μF cm^{-2} per electrode in parallel with a Faradaic resistance of ca. 2 x 10^4 ohm cm^{-2} per electrode gives rise to an extra semi-circle in the complex plane. (The quoted resistance was obtained from the maximum value of Z'' and the capacitance from the frequency at which Z'' passes through its maximum.) For the β phase, which was polycrystalline, the complex plane plot given in Fig. 9c was observed. The plot was essentially the same for data taken in both a H_2 atmosphere and a vacuum [54]. It is consistent with a Warburg type impedance being in series with an *RC* element corresponding to an interfacial polarization, the latter being due to blocking of K^+ and/or F^- charge carriers.

5.3.2 *Intergranular Effects in Polycrystalline Electrolytes*

The effect of intergranular material on the overall electrical response of polycrystalline electrolytes is discussed here. A full account has been given elsewhere [40,56], to which the reader is referred for experimental details.

The simplest representation of intergranular impedance between grains in polycrystalline materials is the circuit shown in Fig. 3a, where one *RC* element is associated with a grain and the other with an inter-granular interface. It has been shown by Armstrong et al [20] that such a series circuit can represent the principle features of polycrystalline electrolytes. The values of the individual components, however, obviously differ from those given in Fig. 3a. Since the interface is thin and has a cross-section area less than the electrical pathways through the grains

themselves, and because the permittivities of most materials vary by less than a factor of 10, the capacitance C_i associated with the interface is much higher than that of the grain, C_p. Since intergranular resistances are a significant problem only when they are larger than those of the grains themselves, the interfacial resistance R_i is greater than that of a typical grain. Thus both the capacitance and resistance of the intergranular material are greater than those of the grains themselves. This is illustrated schematically in Fig. 10a. As before (Fig. 2), the resistivity and modulus spectra primarily reflect the high resistance and low capacitance aspects, respectively, of the total electrical response.

5.3.2 (i) *Intergranular Cracking*.

Experimental M'' and Z'' spectra for a polycrystalline material known to have intergranular cracking are shown in Figs 10b, 10c. The similarity to the response of the simple equivalent circuit is clear, although the experimental peaks are broader. The experimental peaks are approximately the sum of two Debye peaks of equal heights, so that the maxima in Z'' and M'' are approximately equal to *R*/4 and $C_0/4C$ respectively, rather than the values of *R*/2 and $C_0/2C$ appropriate for a Debye peak. The values of *R* and *C* for the intergranular and granular material calculated in this way, assuming the resolution into symmetric ρ'' peaks shown in Fig. 10c, are:

Intergranular (lower frequency) Relaxation

$\tau_i = R_i C_i = 1/\omega_{\max}(Z'') = 6.4\times10^{-6}$ s,

$R_i = 4Z''_{\max} = 6.4\times10^{6}\ \Omega$.

Thus $C_i = \tau_i/R_i = 1.0\times10^{-12}$ F=1.0 pF.

Granular (higher frequency) Relaxation

$\tau_g = R_g C_g = 1/\omega_{\max}(Z'') = 1.6\times10^{-7}$ s .

Thus $C_g = \tau_g/R_g = 6.1\times10^{-14}$ F = 0.061 pF.

After the intergranular cracking was annealed out by heating [40] the impedance spectrum was drastically altered (Fig. l0c). This spectrum is almost indistinguishable from the high frequency resistivity peak in the cracked material, strongly suggesting that it is due to relaxation in the grains themselves. The modulus spectrum is almost unaffected by the annealing, indicating that it is not influenced by the high capacitance intergranular cracking that produced the second frequency peak in the impedance spectrum.

Since the overall conductivity of the cracked sample is determined by the higher resistance intergranular cracks, the ratio of the conductivities of the sample before and after annealing (Fig. 10d) should be the same as the relative heights of the two impedance peaks. This is found to within about 10%, thus justifying the use of a circuit such as that given in Fig. 10a in the analysis of the data. We stress again that the detailed information about the resistivity and capacitance of the intergranular and intragranular relaxations obtained here could not have been obtained, even approximately, from the raw $\sigma'(\omega)$ and $\varepsilon'(\omega)$ data (Fig. 10d). Modulus and impedance spectroscopy thus show up complexities in the electrical

response whose existence may not even be suspected from the conventional log σ' and ε' vs log f plots.

5.3.2. (ii) *Intergranular Gas Adsorption*

The effects of oxygen and alkali doping on the electric response of polycrystalline zinc oxide have been reported by Seitz and Sokoly [57]. Their conductivity and permittivity data were plotted as a function of frequency, thus permitting the modulus and resistivity functions to be calculated, albeit with large uncertainties due to reading errors of ca. 5% in f, σ' and ε'. The uncertainties in M'' and ρ'' are thus about 15%.

The original data for un-doped polycrystalline zinc oxide exposed to an oxygen pressure of 1 atmosphere at 500 K is shown in Fig. 11 (inset), and the derived resistivity and modulus spectra are shown in the main body of Fig. 11. The authors concluded, from the increase in conductivity with decreasing oxygen pressure and the absence of changes due to different electrode materials, that adsorbed oxygen at grain surfaces was responsible for the polarization of the sample.

The modulus and resistivity spectra, that both show two partially resolved peaks, are consistent with a thin, high resistance layer determining the low frequency electrical response. The low and high frequency peaks in M'' have comparable half widths (ca. 1.5 decades), so that their relative heights (8×10^{-4} and 1.1×10^{-2}) are a good measure of the relative capacitances of each relaxation. Thus the capacitance of the low frequency relaxation is about 14 times larger, and from the frequencies at which the maxima occur (about 5×10^{2} and 1×10^{6} Hz) the resistivity of the low frequency process is calculated to be 140 times larger. The conductivity evaluated from the height of the low frequency resistivity peak via eq. (97) is $1.1\pm0.2\times10^{-5}$ S/m, in agreement with the observed low frequency plateau value of $1.3\pm0.1\times10^{-5}$ S/m.

From the relative positions of the modulus peaks, and the relative heights of the (poorly resolved) impedance peaks, the conductivity of the high frequency bulk relaxation is estimated to be between 10^{-6} and 10^{-5} S/m.

Because of its higher capacitance the low frequency relaxation probably corresponds to an intergranular impedance and its removal, e.g. by a reduction in oxygen partial pressure, should therefore increase the sample conductivity by 140 and decrease the permittivity by 14. These numbers are consistent with the stated increase in conductivity and reduction in permittivity with decreasing oxygen pressure, but the magnitudes of these changes were not reported. However, intergranular oxygen is desorbed at high temperatures, and since permittivities are weak functions of temperature it is possible to estimate the measured permittivity in the absence of intergranular polarization from the high temperature data. The data at 800K (dotted line, Fig. 11 inset) indicate a low frequency permittivity that is about 10 times smaller than that at 500K, in decent agreement with the factor of 14 observed from the modulus spectrum.

5.3.2 (iii) *Comparison of Polycrystalline Single Crystal Electrical Relaxations in Sodium Beta Alumina.*

Both polycrystalline and single crystal sodium beta alumina have been studied by Ingram and coworkers [48,62] using impedance and modulus spectroscopy. These studies offer another excellent illustration of the fine details that can be inferred when appropriate formalisms are used for data analysis. The modulus spectra of the polycrystalline form [40, 58, 59], and the single crystal in orientations parallel and perpendicular to the conduction plane [58, 62], are reproduced in Fig. 7. The polycrystalline modulus spectrum is essentially the sum of the two single crystal spectra. Because of the large difference in conductivity between the two orientations, the two components are fairly well resolved in the polycrystalline spectrum. There is no evidence for an intergranular impedance in the polycrystalline modulus spectrum.

5.3.3.*Application of Electric Modulus Spectroscopy to Maxwel-Wagner Interfacial Polarization*.

When spheres of a material with conductivity σ_1 and relative permittivity ε_1 are suspended in a non-conducting medium with relative permittivity ε_2, an interfacial polarization is observed that has a single relaxation time given by

$$\tau_E = \frac{(2\varepsilon_1 + \varepsilon_2)e_0}{\sigma_1}, \tag{106}$$

and a maximum dielectric loss given by

$$\varepsilon''_{\max} = \left(\frac{9\gamma\varepsilon_1^{\,2}}{2(2\varepsilon_1 + \varepsilon_2)}\right)\left[1 + \frac{3\gamma(\varepsilon_2 - \varepsilon_1)}{(2\varepsilon_1 + \varepsilon_2)}\right], \tag{107}$$

where γ is the volume fraction of spheres. These equations are valid only if the spheres do not interact electrically with one another. This dielectric loss phenomenon is known as Maxwell-Wagner polarization [4, 68].

Like other interfacial effects, Maxwell-Wagner polarization may be viewed as a charge build-up between two parallel *RC* elements in series. Thus the single loss peak observed in ε'' should correspond to two peaks in M'' and ρ''. However, for this system the resistance of the suspending medium is essentially infinite, so that only a single peak in M'' and ρ'' reflecting the *RC* loss in the sphere is expected. Their positions and intensities reflect the relaxation of the sphere itself, whereas the dielectric loss also reflects the permittivity of the surrounding medium.

The Maxwell-Wagner effect was observed in emulsions of water in heptanes [68], stabilized by the surfactant sorbitol tristearate. Since water in these emulsions can be routinely supercooled to −35°C, the Maxwell-Wagner effect afforded an opportunity to measure the permittivity and conductivity of super-cooled water. However, as will be seen the emulsifying agent complicated the situation to such an extent that ε'' was of little value, and useful information could only be gained from the M'' spectra. Because the emulsions had a high volume fraction of water (ca. 30%), the modulus also circumvented complications due to

particle interactions at high concentrations. The method of data analysis presented here should be of general utility in analyzing Maxwell-Wagner type polarizations that cannot be studied by the usual dielectric loss method.

The observed dielectric loss spectra for a 30% water emulsion, at 4 temperatures, are shown in Fig. 12a. The maximum loss ε''_{max} decreases with decreasing temperature. This is the reverse of that predicted by eq. (107), because the permittivity ε_1 of water increases with decreasing temperature. Note that $2\varepsilon_1 \gg \varepsilon_2$ for water in heptane emulsions so that

$$\varepsilon''_{max} = \left(\frac{9\gamma\varepsilon_1}{4}\right)\left[1-\frac{3\gamma}{2}\right]. \tag{108}$$

Thus ε''_{max} is directly proportional to ε_1. The modulus spectra are shown in Fig.12b. Their heights also decrease with decreasing temperature, but appropriately so in this case because M''_{max} is proportional to the inverse of the permittivity of the water droplet, i.e. the permittivity increases with decreasing temperature. By comparing M''_{max} at 0°C with the known permittivity of water at that temperature the proportionality constant is fixed and the permittivity at lower temperatures can be determined. The values of ε_1 for water derived from a least squares quadratic fit to 8 data points between 0°C and −35°C are compared with the values derived from the observed permittivity of a dilute suspension of water droplets in a polymeric emulsifier (69) in Table 1. For clarity, only half of these data are plotted in Figure 12. The agreement is well within the ±2% uncertainties of each method, thus confirming that the modulus formalism is indeed valuable for the analysis of Maxwell-Wagner polarization. When the water-in-heptane data are normalized to produce the same average as reference [70] the agreement improves to $\pm 0.5\%$.

Table 1
Relative permittivity of supercooled water

Temperature (^{o}c)	**(a)**	**(b)**	**(c)**	**(a)-(c) (%)**
-35	107.7	105.9	107.3	+0.4
-30	104.2	102.8	104.1	+0.1
-25	100.8	99.8	101.1	-0.3
-20	98.3	97.1	98.4	-0.1
-15	95.6	94.5	95.7	-0.1
-10	93.4	92.1	93.3	+0.1
-5	90.9	89.9	91.1	-0.2
Average	98.7	97.4	98.7	0

(a) Reference [70]
(b) Reference [69]
(c) Reference [69] after adjustment of average

5.4. *Conductivity and Dielectric Relaxation in the Temperature Domain.*

To illustrate the points raised in §3.6 it is desirable that a material exhibit both dielectric and conductivity relaxations. Hydrated ionic glasses fulfill this need since they exhibit dielectric relaxation of water below T_g and an ionic conductivity relaxation near T_g. The temperature dependences of ε'', ε', $\tan\delta$, M'' and ρ'' taken at 1 Hz for a monomeric hydrate glass [24] are shown in Fig. 13. We discuss several features of these spectra. First, it is apparent that Z'' is featureless in the temperature domain and contains little information. This is a reflection of $\ln\omega$ and E_A/RT not being equivalent variables for this function. For a single relaxation time this can be made explicit:

$$\begin{aligned}\rho'' = \frac{M''}{e_0\omega} &= \left(\frac{\tau}{e_0\varepsilon'}\right)\left(\frac{\omega\tau}{1+\omega^2\tau^2}\right) && \text{peak in } \omega \text{ domain,}\\ &= \left(\frac{1}{\omega e_0\varepsilon'}\right)\left(\frac{\omega^2\tau^2}{1+\omega^2\tau^2}\right) && \text{no peak in } \tau \text{ domain.}\end{aligned} \tag{109}$$

The observed decrease in Z'' in the vicinity of the conductivity relaxation (where $\tan\delta \approx 1$ and M'' passes through its high temperature maxima), is due to Z'' being proportional to M' at constant frequency (eq. (109)) and the decrease in M' with decreasing 1/*T* in the conductivity relaxation region.

Of the remaining loss functions, there is a steady increase in resolution in going from ε'', to $\tan\delta = \varepsilon''/\varepsilon'$ to $M'' \approx \varepsilon''/\varepsilon'^2$ (eq. 55). This is due to the gradual increase in ε' offsetting the more or less steady rise in ε'' as the temperature increases.

The resolution of the conductivity and dielectric relaxations improves with decreasing frequency for the data given in Fig. 13 (not shown). This is usually the case, but exceptions do occur. An example of the latter was found for an ion containing polymer, in which the resolution of the dielectric loss from the conductivity background improves with *increasing* frequency. This occurred because the activation energy for conductivity in this case was smaller than that of the dielectric loss, and yet the conductivity relaxation occurred at a higher temperature (lower intrinsic frequency). For the aqueous glass just discussed [24] the activation energy for conductivity is higher because the material is ionic and the high activation energy for viscous flow ("structural" relaxation) in the glass transition region is included in the conductivity activation energy.

Masking of a dielectric relaxation by a high background conductivity at all accessible frequencies has often been observed. An illustration of the effect in the temperature domain is shown in Fig. 14, where the dielectric relaxation of a glassy aqueous solution of a lithium salt is masked to an increasing extent by the increased conductivity accompanying the substitution of protons for lithium ions. A similar effect was observed by Howell [23], where the dielectric relaxation of glycerol was masked by the conductivity of dissolved lithium chloride.

The effect of activation energy on the relaxation width in the temperature domain is also illustrated in Fig. 14. The modulus spectrum of the pure acid is wider on a l/*T* scale than those of the lithium containing materials, because the activation energy for conductivity is lower for the acid. When the spectra are plotted as a function of $\langle E_A \rangle / RT$ in Fig. 14 inset, the (lower frequency) conductivity relaxations are seen to be of comparable widths. However, the higher frequency secondary relaxations are characterized by lower average activation energies, so that

the E_A/RT scale is not applicable to them. This overlap of temperature scales that are normalized by different average activation energies is a major source of difficulty in the analysis of relaxation in the temperature domain.

Concluding Remarks

It is apparent from the different applications of the various relaxation formalisms described in section 4 that, generally speaking, the impedance formalisms best ρ^* and M^* are suited for the analysis of ac conductivity of conducting electrolytes. For the extrapolation of electrode polarization effects to get data relevant to the bulk electro1yte the complex impedance plane is the most useful method of analysis. For bulk relaxation effects, including those due to intergranular impedances, spectra of ρ'' and M'' together appear to be the most useful. If the bulk relaxation is to be analyzed with minimal interference from interfacial effects, whether these are at the electrode interface, grain boundaries or other sources, the electric loss modulus is unsurpassed. The examples cited indicate again that a large amount of the information contained in experimental ac data can be lost if the wrong method of data analysis is employed.

Acknowledgements

The author is indebted to a number of colleagues for their help in clarifying many of the concepts discussed here. They include Dr. M. D. Ingram, Professor A. Eisenberg, Professor C. T. Moynihan, and Professor C. A. Angell. Special thanks are also due to Professor Angell for providing the clerical facilities without which this article would not have been completed.

References

1. Y. F. Yao and J. 1. Kimmer, *J. Inorg. Nuci. Chem*. 29, 2453 (1967).

2. J. G. Berberian and R. H. Cole, *Rev. Sci. Instrum*. 40, 811 (1969).

3. A. Kyrala, "*Applied Functions of a Complex Variable*", Wiley-Interscience (1972).

4. J. C. Maxwell, '*Electricity and Magnetism*," 3rd Edition, Oxford Univ. Press (1892).

5. P. Debye, "*Polar Molecules,*" Chemical Catalog Co., New York (1929).

6. (a) H. E. Taylor, *Trans. Faraday Soc.* 52, 873 (1956).

   (b) H. E. Taylor, *J. Soc. Glass Technol*. 41, 350 (1957).

7. J. M. Stevels, *Handbuch der Physik*, Vol XX 372 (1957).

8. H. E. Taylor, *J. Soc. Glass Technol*. 43, 124 (1959).

9. R. J. Charles, *J. Appl. Phys.* 32, 1115 (1961).

10. J. 0. Isard, *Proc. Inst. Elect. Engrs*., *Supplement No. 20*, 109B, 440 (1962).

11. J. 0. Isard, *J. Non. Cryst. Solids* 4, 357 (1970).

12. D. Ravain and J.-L Souquet, *J. Chim. Phys*. 71, 693 (1974).

13. B. V. Elamon, *Proc. Inst. Electr. Engrs*. 99, 151 (1952).

14. G. Williams, D. C. Watts, S. B. Dev and A. M. North, *Trans. Faraday Soc*. 67 1323 (1971).

15. N. E. Hill, W. E. Vaughn, A. H. Price and M. Davies, '*Dielectric Properties and Molecular Behavior*," p. 112, Van Nostrand (1969).

16. N. G. McCrum, B. E. Read and G. Williams, '*Anelastic and Dielectric Effects in Polymeric Solids," Wiley (1967).*

17. L. Hayler and M. Goldstein, *J. Chem. Phys*. 66, 4736 (1977).

18. P. B. Macedo, C. T. Moynihan and R. Bose, *Phys. Chem. Glasses* 13, 171 (1972).

19. C. Kittel, "*Introduction to Solid State Physics*," 4th Ed., Wiley, (1971).

20. R. D. Armstrong, T. Dickinson and P. M. Willis, *J. Electroanal. Chem*. 53, 389 (1974).

21. I. M. Hodge, M. D. Ingram and A. R. West, *J. Electroanal. Chem*. 58, 429 (1975).

22. J. H. Ambrus, C. T. Moynihan and P. B. Macedo, *J. Phys. Chem*. 76, 3287 (1972).

23. F. S. Howell, *Ph.D. Thesis*, Catholic University of America (1972).

24. I. M. Hodge and C. A. Angell, *J. Phys. Chem*. 82 1761 (1978)

25. H. P. Schwan, G. Schwarz, J. Maczak and H. Pauly, *J. Phys. Chem*. 66, 2626 (1962).

26. R. D. Armstrong, W. P. Race and H. R. Thirsk, *Electroshim Acta*. 13, 215 (1968).

27. J. Braunstein and G. D. Robbins, *J. Chem. Educ*. 48, 52 (1971).

28. D. Miliotis and D. N. Voon, *J. Phys. Chem. Solids* 30, 1241 (1969).

29. J. M. Wimmer and N. M. Tallan, *J. Appl. Phys*. 37, 3728 (1966).

30. (a) T. M. Proctor and P. M. Sutton, *J. Am. Ceram. Soc*. 43, 173 (1966).

(b) P. M. Sutton, ibid, 67, 188 (1966).

31. (a) E. Warburg, *Wied. Ann.* 67, 493 (1899).

(b) E. Warburg, *Ann. Phys*. 6, 125 (1901).

32. I. Fried, "The Chemistry of Electrode Processes," Academic (1973).

33. R. D. Armstrong, *J. Electroanal. Chem*. 52, 413 (1974).

34. J. Bruinink and G. H. J. Broors, *J. Phys. Chem. Solids* 33, 1713 (1972).

35. A. K. Jonscher, *Nature* 267, 673 (1977).

36. A. K. Jonscher, *Nature* 253, 717 (1975).

37. D. C. Salter, *Nature* 271 *645* (1978).

38. J. E. Bauerle, *J. Phys. Chem. Solids* 30, 2657 (1969).

39. R. D. Armstrong and R. A. Burnham, *J. Electroanal. Chem*. 72, 257 (1976).

40. C. G. Koops, *Phys. Rev.* 83, 121 (1951).

41. I. M. Hodge, M. D. Ingram and A. R. West, *J. Electroanal. Chem*. 74, 125 (1976).

42. M. Pollak and T. H. Geballe, *Phys. Rev.* 122, 1742 (1961).

43. X. LeCleach and J. F. Palmier, *J. Non Cryst. Solids* 18, 265 (1975).

44. D. Ravairie, J. P. Diard and J. -L. Souquet, *Faraday Trans. II*, 1935 (1975).

45. I. M. Hodge and C. A. Angell, *J. Chem. Phys*. 67, 1647 (1977).

46. D. W. Davidson, *Can. J. Chem*. 39, 571 (1961).

47. K. S. Cole and R. H. Cole, *J. Chem. Phys*. 9, 341 (1949).

48. R. J. Grant and M. D. Ingram, *J. Electroanal. Chem*. 83, 199 (1977).

49. M. Sluyters Rehback and J. H. Sluyters, in "Electroanalytical Chemistry," Vol. 4, p. 7, Ed. A. J. Bard, Marcel Dekker (1970).

50. (a) R. D. Armstrong and R. Mason, *J. Electroanal. Chem*. 41, 231 (1973).

(b) R. D. Armstrong and W. I. Archer, *ibid*, 87, 221 (1978).

51. R. D. Armstrong, T. Dickinson and P. M. Willis, *J. E1ectroanal. Chem*. 48, 47 (1973).

52. R. D. Armstrong, T. Dickinson and P. M. Willis, *J. Electroanal. Chem*. 54, 281 (1975)

53. R. D. Armstrong and K. Taylor, *J. Electroanal. Chem*. 63, 9 (1975).

54. J. Bruinink, *J. Electroanal. Chem*. 51, 141 (1974).

55. J. Bruinink and G. H. J. Broers, *J. Phys. Chem. Solids* 33, 1713 (1972).

56. A. B. Lidiard, "*Handbuch der Physik*", Vol. XX, 312, Springer-Berlin (1957).

57. I. M. Hodge, M. D. Ingram and A. R. West. *J. Amer. Ceram. Soc*. 59, 360 (1976).

58. M. A. Seitz and T. L. Sokoly, *J. Electrochem. Soc*. 121, 163 (1974).

59. R. J. Grant, M. D. Ingram, and A. R. West, *J. Electroanal. Chem*. 72, 397 (1976).

60. R. J. Grant, M. 0. Ingram and A. R. West, *Electrochim. Acta* 22, 729 (1977).

61. I. M. Hodge, R. J. Grant, M. D. Ingram and A. R. West, *Nature* 266, 42 (1977).

62. I. M. Hodge, R. J. Grant, M. D. Ingram and A. R. West, *J. Am. Ceram. Soc*. 60, 266 (1977).

63. R. J. Grant and M. D. Ingram. *J. Electroanal. Chem*. 83, 199 (1977).

64. M. S. Whittingham and R. A. Huggins, *NBS Special Publication*, 364, 139 (1972).

65. L. Page and N. J. Adams, "*Principles of Electricity*", 2nd Edition, 64, Van Nostrand, New York (1949).

66. J. Frenkel, "*Kinetic Theory of Liquids*," Dover (1955).

67. W. Bailey, S. Glowinkowski, H. Story and W. L. Roth, *J. Chem. Phys*. 64, 4126 (1976).

68. K. W. Wagner, *Arch. Electrotechn*. 2, 371 (1914).

69. I. M. Hodge and C. A. Angell, *J. Chem. Phys*. 68, 1363 (1978)

70. J. B. Hasted and M. Shahadi, *Nature* 262, 777 (1976).

71. I. M. Hodge and A. Eisenberg, *Macromolecules* ,11 283 (1978).

72. G. Williams and D. C. Watts, *Trans. Faraday Soc.* 66, 80 (1970).

73. D. W. Davidson and R. H. Cole, *J. Chem. Phys*. 18, 1417 (1951).

74. W. Weibull, *Ing. Veterskap. Akad. Handl*. No. 153 (1939).

75. W. Weibull, *Ceram. Abstr*. 19, 293 (1951).

76. W. Weibull, *J. Appl. Mech*. 18, 293 (1951).

77. R. W. Douglas in "*Amorphous Materials*", Ed. R. W. Douglas and B. Ellis, Wiley, New York (1972).

78 C. T. Moynihan, personal communication

FIGURE CAPTIONS

Figure 1 Equivalent circuit for a Debye dielectric relaxation. G_0 is the zero frequency conductance, and C_0 the high frequency limiting capacitance. The relaxation behavior is simulated by the series conductance and capacitance in the lowest arm of the circuit. τ is the dielectric relaxation time.

Figure 2 Spectra of the four basic relaxation functions for a representative equivalent circuit where ω is the angular frequency in radian $\sec^{-1}$. Single primed symbols refer to real components, double primed symbols to imaginary components.

(A) Equivalent circuit.

(B) Spectra of the components of the complex conductivity σ^* . The high and low frequency relaxation limits of the real component are shown (σ_∞ and σ_0 respectively). The spectrum of σ'' with its high frequency limit σ_∞ (proportional to ω) subtracted is also shown.

(C) Spectra of the components of the complex relative permittivity ε^*. The spectrum of ε'' with the zero frequency conductivity contribution $\sigma_0/\mathrm{e}_0\omega$ subtracted out, is also shown. Note the logarithmic scale for ε^* at low frequencies, and linear scale at high frequencies.

(D) Spectra of the components of the complex resistivity ρ^*. Logarithmic scales are given in the insets to indicate the presence of the high frequency peak in ρ'' at low frequencies.

(E) Spectra of the components of the complex electric modulus, *M**. The non-zero low frequency limit of *M'* is shown at left.

Figure 3 Complex plane plots for the circuit and spectra of Figure 2.

(A) Complex conductivity plane. The low frequency relaxation due to C_s is shown in the inset (note different scale).

(B) Complex relative permittivity plane. Note the different scales for the low frequency (upper) and high frequency (lower) relaxations.

(C) Complex resistivity plane. Note different scales for each part.

(D) Complex modulus plane.

Figure 4 Arrhenius plot for conductivity of Li4GeO4 at different fixed measuring frequencies. The dotted line gives the expected high temperature behavior (not measured). Data are for (Ref. [57]).

Figure 5 Complex admittance plane behavior of polycrystalline yttria-zirconia solid electrolytes, after Bauerle (ref. [37]).

(A) Equivalent circuit used in data processing.

(B) Complex admittance plane for circuit given in (A). The relations between the complex plane parameters and the circuit elements are given at the bottom of the figure.

(C) Experimental complex admittance plane behavior. Each relaxation conforms to the Cole-Cole function (see Appendix A2-3). The angles θ measure the displacement of the semicircle centers below the real axis and are related to the width parameter α $\left(\alpha = \theta / 90^{\circ}\right)$. Four terminal (4T) and direct current (dc) data are indicated. The upper numbers refer to the measuring frequency in Hz.

Figure 6 Relaxation functions for the proton conducting glass $HZnC1_3 \bullet 4H_20$ at −105°C (ref [45]).
(A) Spectra of the specific conductivity σ', relative permittivity ε' and electric loss modulus M''. Circles are data points, and solid lines are for the best fit Davidson-Cole function for M''. Davidson-Cole parameters (see Appendix A2-1) are $M_\infty = 0.105$, $\gamma = 0.33$, $\tau_0 = 1.07 \times 10^{-3}$ sec.
(B) Resistivity spectrum. Solid line is spectrum derived from Davidson-Cole function for M''. Circles are observed data points and the dotted line is hand-drawn through the data.
(C) Complex resistivity plane plot. The solid semicircle is calculated from the Davidson-Cole function for M''. The low frequency polarization extrapolation is also shown.

Figure 7 Spectra for single crystal and polycrystalline $\beta-$alumina at −160°C (after Ingram et al. , refs. [48, 60-62]).
(A) Electric loss modulus spectra for single crystal in orientations parallel and perpendicular to conduction plane.
(B) Dielectric loss spectra for single crystal in same orientations as (A).
(C) Electric loss modulus and impedance spectra for single crystal. Open circles are M'' parallel to conduction planes, closed circles are M'' in the perpendicular orientation, and dotted line is Z'' in the parallel orientation.
(D) Electric loss modulus and impedance spectra for polycrystalline $\beta-$alumina (ref. [48]). Note the coincidence of two resolvable modulus peaks with the crystal spectra for the two orientations shown (A).

Figure 8 Complex impedance plane data at room temperature for 2 sintered polycrystalline $\beta-$alumina preparations (after Armstrong et al, Ref. 20).
(A) Sinter 1 (see ref. [20] for preparation details).
(B) Sinter 2, with different surface preparations. Note that the high frequency extrapolations give self-consistent values for σ_0.

Figure 9 Complex impedance plane plots for KHF_2 (after Bruinink Ref. 54).
(A) Single crystal $\alpha-KHF_2$, in an atmosphere of H_2.
(B) Single crystal $\alpha-KHF_2$, in vacuo. Inset gives the low frequency relaxation due to electrode polarization.
(C) Polycrystalline $\alpha-KHF_2$.

Figure 10 Relaxation spectra for a cracked and an annealed polycrystalline preparation of a lithium ion solid electrolyte (after Hodge et al, ref. [41]).
(A) Impedance and modulus spectra for the indicated equivalent circuit.
(B) Modulus spectra of cracked (1), partially annealed (2), and fully annealed (3) material.
(C) Impedance spectra corresponding to data given in (B). Note the disappearance of the low frequency relaxation with annealing. The dotted lines are a resolution assuming the low frequency relaxation to be symmetric.
(D) Conductivity spectra corresponding to data given in (B) and (C). Note the great loss of information compared with the spectra given in C.

Figure 11 Relaxation spectra for polycrystalline zinc oxide in 1 atm O_2 (after Seitz and Sokoly, ref. [58]). Note logarithmic ordinate scales. Circles are data points at 500 K. Dotted line in inset is permittivity spectrum at 800 K.

Figure 12 Temperature dependences of dielectric loss spectra (A) and electric loss modulus spectra (B) of water droplets in heptane-$CC1_4$ emulsions (after Hodge and Angell, ref. [69]). Open and closed circles and open and closed squares are data at 0°, −9.8°, −21.4° and −35.0°C, respectively.

Figure 13 Relaxation functions in the temperature domain for $Ca(NO_3)_2.4H_2O$ at 1 Hz (after Hodge and Angell, ref. [24]).

Figure 14 Electric loss moduli versus reciprocal temperature for a series of glassy Li salt/acid mixtures, illustrating the masking of the secondary relaxation in Li salt by the conductivity of the acid (Ref. 45). Inset: The same data as a function of E_A / RT, where E_A is the average activation energy for the (high temperature) conductivity relaxation. Δ denotes shifts of spectra to make the conductivity relaxations coincide.

Figure A2-1 Definition of electric loss modulus parameters.

Figure A2-2 Comparison of Cole-Cole resistivity spectrum (closed circles) with the spectrum derived from Davidson-Cole M'' spectrum (open circles). Note the two frequency scale corresponding to shifts made to make half height points coincide. The Cole-Cole function has been normalized to make ρ''_{max} coincide with that of the Davidson-Cole function.

Figure A3 Definitions of limiting relative permittivities for dielectric and conductivity relaxations.

APPENDICES

Appendix A1 Summary of Relaxation Formalisms and their Limiting Values

1 (a) Cell constant $\equiv k = \ell / A$ for parallel plate electrodes of area A separated by ℓ

(b) Geometric capacitance $\equiv C_0 = \mathrm{e}_0 / k$

2 Relationships Between Functions

$$M^* = 1/\varepsilon^* = i\,\mathrm{e}_0\,\omega\rho^* = i\,C_o\,\omega Z^*$$

$$\rho^* = 1/\sigma^* = 1/\left(i\,\mathrm{e}_0\,\omega\varepsilon^*\right)$$

$$\sigma^* = i\,\mathrm{e}_0\,\omega\varepsilon^*$$

3. Function definitions in terms parallel conductance $G_p = 1/R_p$ and capaitance C_p

(a) Permittivity $\varepsilon^* = \varepsilon' - i\,\varepsilon''$

$$\varepsilon' = C_p / C_0$$

$$\varepsilon'' = G_p / C_0\,\omega$$

$$\lim_{\omega\to 0}\left(\varepsilon'\right) = \varepsilon_0 \quad \text{(conductivity relaxation)}$$

$$= \varepsilon_U \quad \text{(dielectric relaxation)}$$

$$\lim_{\omega\to\infty}\left(\varepsilon'\right) = \varepsilon_\infty \quad \text{(conductivity relaxation)}$$

$$= \varepsilon_R \quad \text{(dielectric relaxation)}$$

(b) Conductivity $\sigma^* = \sigma' + i\,\sigma''$

$$\sigma' = \mathrm{e}_0\,\omega\varepsilon'' = k\,G_p$$

$$\lim_{\omega\to 0}\left(\sigma'\right) = \sigma_0 \quad \text{(conductivity relaxation)}$$

$$= 0 \quad \text{(dielectric relaxation)}$$

$$\sigma'' = \mathrm{e}_0\,\omega\varepsilon' = k\omega C_p$$

$$\lim_{\omega\to\infty}\left(\sigma'\right) = \sigma_\infty \quad \text{(conductivity relaxation)}$$

$$= \sigma_R \quad \text{(dielectric relaxation)}$$

(c) Electric Modulus $M^* = M' + i\,M''$

$$M' = \frac{\varepsilon'}{\varepsilon'^2 + \varepsilon''^2} = \left(\frac{C_0}{C_p}\right)\frac{\omega R_p^2 C_p^2}{1+\omega R_p^2 C_p^2} = \frac{\varepsilon'}{1+\tan^2\delta}$$

$$M'' = \frac{\varepsilon''}{\varepsilon'^2 + \varepsilon''^2} = \left(\frac{C_0}{C_p}\right)\frac{\omega R_p C_p}{1+\omega R_p^2 C_p^2} = \frac{\tan\delta}{\left(1+\tan^2\delta\right)\varepsilon'}$$

$$\lim_{\omega\to 0}\left(M'\right) = 0 \quad \text{(conductivity relaxation)}$$

$$= 1/\varepsilon_U \quad \text{(dielectric relaxation)}$$

$$\lim_{\omega\to\infty}\left(M'\right) = M_\infty = 1/\varepsilon_\infty \quad \text{(conductivity relaxation)}$$

$$= 1/\varepsilon_R \quad \text{(dielectric relaxation)}$$

Appendix A2 Specific Distribution Functions

There are a large number of distribution functions that are used to describe experimental dielectric loss data, and some of the more common ones used for conductivity relaxations are summarized here. The functions are defined, where possible, in terms of $M^*(i\omega)$, $\phi(t)$ or $\frac{d\phi(t)}{dt}$, and $g(\ln\tau)$. The moments of $g(\ln\tau)$ are also given, where possible. Relations giving the parameters of the functions in terms of features of the corresponding loss spectrum (imaginary component as a function of frequency) are also given. The spectrum features are defined in Figure A2-1.

When fitting a distribution function for ε^* or to M^*, it must be recognized that their real components differ. For normalized functions, in which the dispersion in the real component is unity, the relations are:

$M' \leftrightarrow 1-\varepsilon' \leftrightarrow 1-\rho' \leftrightarrow \sigma'$

A2-1 Davidson-Cole Function

1.

$(0<\gamma\le 1);\ \phi=\arctan(\omega\tau_0)$

$$M^*=\frac{M_\infty}{1-(1-i\omega\tau_0)^{-\gamma}}$$

$$M'=M_\infty\left[1-(\cos\phi)^\gamma\cos(\gamma\phi)\right]$$

$$M''=M_\infty\left[1-(\cos\phi)^\gamma\sin(\gamma\phi)\right]$$

[CHECK]

2.

$$-\frac{d\phi}{dt}=\left[\frac{1}{\tau_0\Gamma(\gamma)}\right]\left(\frac{t}{\tau_0}\right)^{\gamma-1}\exp\left(-\frac{t}{\tau_0}\right),\ \text{where } \Gamma \text{ is the gamma function.}$$

=

3.

$$g(\ln\tau)=\left(\frac{1}{\pi}\right)\sin(\gamma\pi)\left(\frac{\tau}{\tau_0-\tau}\right) \qquad \tau<\tau_0$$

$$=0 \qquad \tau\ge\tau_0$$

4.

$$\left\langle \tau^n \right\rangle = \tau_0^n \left[\frac{\Gamma(n+\gamma)\Gamma(1-\gamma)}{\Gamma(n+1)} \right] \frac{\sin(\gamma\pi)}{\pi}$$

$$= \frac{\tau_0^n}{n} \left[\frac{\Gamma(n+\gamma)}{\Gamma(n)\Gamma(\gamma)} \right] \qquad \text{where } B(n,\gamma) \equiv \frac{\Gamma(n)\Gamma(\gamma)}{\Gamma(n+\gamma)} \text{ is the beta function.}$$

$$= \frac{\tau_0^n}{n} \left[\frac{1}{B(n,\gamma)} \right]$$

Special cases:

$$n=1: \langle \tau \rangle = \gamma \tau_0; \quad n=2: \left\langle \tau^2 \right\rangle = \left(\frac{\tau_0^2}{2} \right) \gamma(1+\gamma)$$

5.

$$\gamma^{-1} \approx -1.2067 + 1.6715\Delta + 0.222569\Delta^2 \qquad (1.14 \le \Delta \le 0.31; 0.15 \le \gamma \le 1.00)$$

Gives γ to ±0.002 for $\gamma \le 0.9$, too high by 0.007 at $\gamma = 1$.

6.

(a) $$M'_{\max} = M_\infty (\cos\phi_{\max})^\gamma \sin(\gamma\phi_{\max}) = M_\infty \sin\left(\frac{\gamma\pi}{2(1+\gamma)} \right)^{1+\gamma}$$

where $\phi_{\max} = \dfrac{\pi}{2(1+\gamma)}$.

(b) $$M'_{\max} = M_\infty \left(0.07571 + 0.68277 \cdot \gamma - 0.26176 \cdot \gamma^2 \right).$$

Gives $M'_{\max}$ to ± 0.003 (< 2%) for $0.2 \le \gamma \ge 1.0$

7. $$\tau_0 = \frac{\tan\phi_{\max}}{\omega_{\max}}$$

8.

$$\log_{10}\tau_0 \approx -0.9276 + \frac{0.76486}{\gamma} - \frac{0.056511}{\gamma^2} - \log_{10} f_{1/2}^+$$

where $f_{1/2}^+$ is the upper frequency at which $M'' = M''_{\max}/2$

Gives $\log_{10}\tau_0$ to ± 0.01

9.

$$\log_{10}\tau_0 \approx -1.586 + \frac{0.25915}{\gamma} - \frac{0.035695}{\gamma^2} - \log_{10} f_{1/2}^-$$

where $f_{1/2}^-$ is the lower frequency at which $M'' = M''_{max}/2$

Gives $\log_{10}\tau_0$ to ± 0.01

A2-2. Williams-Watts

The first physical application of this function appears to be a statistical theory of rupture by Wibull [73-75] and the time derivative is referred to as the Weibull distribution function in some statistics compilations. Its application to mechanical relaxation phenomena in inorganic glasses has been reviewed by Douglas [77], and its application to dielectric relaxation was initiated by Williams and Watts [14,72]

1.

$$\phi(t) = \exp\left[-\left(\frac{t}{\tau_0}\right)^{\beta}\right] \qquad (0 < \beta \le 1)$$

$$-\frac{d\phi}{dt} = \left(\frac{\beta}{t}\right)\left(\frac{t}{\tau_0}\right)^{\beta} \exp\left[-\left(\frac{t}{\tau_0}\right)^{\beta}\right] = \left(\frac{\beta}{\tau_0}\right)\left(\frac{t}{\tau_0}\right)^{\beta-1} \exp\left[-\left(\frac{t}{\tau_0}\right)^{\beta}\right]$$

2.

$$M^*(i\omega) = M_\infty \sum_1^\infty (-1)^{n-1}\left[\frac{\Gamma(n\beta+1)}{\Gamma(n+1)}\right]\left(\frac{1}{i\omega\tau_0}\right)^{n\beta}$$

$$M^*(i\omega) = M_\infty \sum_1^\infty (-1)^{n-1}\left[\frac{\Gamma(n\beta+1)}{\Gamma(n+1)}\right]\left(\frac{1}{\omega\tau_0}\right)^{n\beta}\left[\cos(n\beta\pi) + i\sin(n\beta\pi)\right]$$

3. For $\beta = 0.5$ [3a]

$$M^*(iz) = M_\infty\left[\frac{1-\pi^{1/2}(1+i)}{\xi}\right]\exp(-z^2)\operatorname{erfc}(iz)$$

where $\xi = (8\omega\tau_0)^{1/2}$, $z = \frac{1-i}{\xi}$, and erfc is the complementary error function. The function $\exp(-z^2)\operatorname{erfc}(iz)$ is frequently tabulated and included in software packages.

4. Hamon Approximation

$$M''(\omega) = M_\infty \beta \left(\frac{\pi}{5}\right)^{\beta-1} \left(\frac{1}{\omega\tau_0}\right)^{\beta} \exp\left[-\left(\frac{\pi}{5\omega\tau_0}\right)^{\beta}\right] \quad (\omega\tau_0 > 1)$$

Approximation improves as β decreases and $\omega\tau_0$ increases.

5.

$$\langle \tau^n \rangle = \left(\frac{\tau_0^n}{\beta}\right)\Gamma\left(\frac{n}{\beta}\right) = \left(\frac{\tau_0^n}{n}\right)\Gamma\left(1+\frac{n}{\beta}\right) \qquad (n \geq 1)$$

6.

$$\frac{1}{\beta} \approx -0.98984 + 0.96479\Delta - 0.004604\Delta^2$$

Gives β to ± 0.001 for $\beta \leq 0.70$ and within ± 0.002 for $\beta \geq 0.95$

7.

$$M''_{\max} = M_\infty \left(-.0065 + 0.61368\beta - 0.10561\beta^2\right)$$

Gives $M''_{\max} / M_\infty$ to ± 0.01 for $0.3 \leq \beta \leq 1$

8.

$$\log_{10} \tau_0 \approx -1.001 + 0.40882\beta^2 - 0.2048\beta^4 - \log_{10} f_{\max}$$

[Since this paper was written, Lindsay and Patterson [*J. Chem. Phys.* 73 3348 (1980)], published the expression $\log_{10}(\omega\tau_0)_{\max} \approx -0.2307 + 0.386425\beta^2 - 0.16086\beta^4$, corresponding to $\log_{10} \tau_0 = -1.029 + 0.40882\beta^2 - 0.2048\beta^4 - \log_{10} f_{\max}$]

[CHECK AGREEMENT]

9.

$$\log_{10} = -0.8621 + 0.527137\beta^2 - 0.0144123048\beta^4 - \log_{10} f^-_{1/2}$$

10.

$$\log_{10} = -0.7675 + 0.50924\beta^2 - 0.019872\beta^4 - \log_{10} f^+_{1/2}$$

A2-3. Cole-Cole Function [47]

1.

$$M^* = M_\infty \left\{ 1 - \frac{1}{\left[1 + (i\omega\tau_0) 1-\alpha \right]} \right\}$$

$$M' = \frac{M_\infty}{2} \left\{ 1 + \frac{\sin(\alpha\pi/2)}{\left[\cosh(\theta) + \sin(\alpha\pi/2) \right]} \right\} \qquad \theta = (1-\alpha)\ln(\omega\tau_0)$$

$$M'' = \frac{M_\infty}{2} \left\{ 1 + \frac{\cos(\alpha\pi/2)}{\left[\cosh(\theta) + \sin(\alpha\pi/2) \right]} \right\} \qquad \theta = (1-\alpha)\ln(\omega\tau_0)$$

$$= M_\infty \cos(\beta\pi/2) \left[(\omega\tau_0)^{1-\alpha} + (\omega\tau_0)^{-(1-\alpha)} + 2\sin(\alpha\pi/2) \right]$$

[CHECK]

2.

$$g(\ln\tau) = \left(\frac{1}{\pi}\right)\left(\frac{\tau_0}{\tau}\right)^{1-\beta} \left[\frac{\sin(\alpha\pi)}{1 - 2\left(\frac{\tau_0}{\tau}\right)^{1-\alpha} \cos(\alpha\pi) + \left(\frac{\tau_0}{\tau}\right)^{2(1-\alpha)}} \right]$$

3.

$$-\left(\frac{d\phi}{dt}\right) = \left[\frac{\alpha}{\tau_0 (\Gamma(1+\alpha))} \right] \left(\frac{t}{\tau_0}\right)^{-(1-\alpha)} \qquad (t/\tau_0 \ll 1)$$

$$= \left[\frac{\alpha}{\tau_0 (\Gamma(1+\alpha))} \right] \left(\frac{t}{\tau_0}\right)^{-(1+\alpha)} \qquad (t/\tau_0 \gg 1)$$

4.

$$M''_{\max} = M_\infty \left[\sec(\alpha\pi/2) - \tan(\alpha\pi/2) \right]$$

5.

$$\tau_0 = 1/\omega_{\max}$$

6.

$$\frac{1}{1-\alpha} = 0.242106 + 0.648435\Delta + 0.0098624\Delta^2$$

Gives α to ± 0.002 $(0 \le \alpha \le 0.70)$

A2-4. Resistivity Function from Davidson-Cole Electric Modulus

The parameters M_∞, τ_0, γ refer to the Davidson-Cole modulus function.

1.

$$\rho'' = \rho_0 \left\{ \frac{\left[1 - (\cos\phi)^\gamma \cos(\gamma\phi) \right]}{\gamma \omega \tau_0} \right\}$$

where $\rho_0 = \dfrac{M_\infty \gamma \tau_0}{e_0} = \dfrac{1}{\sigma_0} = \dfrac{M_\infty \langle \tau \rangle}{e_0}$ $\qquad \phi = \arctan(\omega\tau_0)$

2.

$$\gamma^2 \approx 49.84439 - 75.526329\Delta + 28.691692\Delta^2$$

where γ is the Davidson-Cole modulus function and Δ is the width at half-height (in decades of frequency) of the ρ'' spectrum. Gives γ to ±0.007 for $0.4 \le \gamma \le 1$; $1.144 \le \Delta \le 1.287$

3.

$$\log_{10}(\tau_0) = -0.5076 - 0.387125\gamma + 0.097606^2 - \log_{10}(f_{max})$$

Gives $\log_{10}(\tau_0)$ to ±0.001 $\quad 0.1 \le \gamma \ge 1.0$

f_{max} refers to the ρ'' spectrum; τ_0 and γ to the Davidson-Cole M'' spectrum.

4.

$$\rho''_{max} = \rho_0 (0.40396 + 0.13135\gamma - 0.03568\gamma^2)$$

Gives ρ''_{max} to ±0.0003 $\quad 0.1 \le \gamma \ge 1.0$

5.

$$\alpha \approx 0.1699 - 0.238106\gamma + 0.068424\gamma^2$$

This relates α for the Cole-Cole resistivity function having the same half width as the resistivity function derived from a Davidson-Cole modulus function with shape parameter γ. Gives α to ± 0.002 $\quad 0.1 \le \gamma \ge 1.0$.

6.

A comparison of a Cole-Cole ρ'' spectrum with that derived from a Davidson-Cole M'' spectrum is given in Fig. A2.2. The two are seen to be very similar, despite the large asymmetry of the Davidson-Cole function $(\gamma = 0.2)$.

Appendix A3

The new nomenclature for limiting low and high frequency limits for conductivity and dielectric relaxations is illustrated in Figure A3.1. Note that this nomenclature for dielectric relaxation differs slightly from that used in reference [16], in order to avoid more confusion rather than add more. The subscript *U* is used to denote low frequency limits for both relaxation and retardation functions, and *R* is used to denote high frequency limits for both relaxation and retardation functions

FIGURE CAPTIONS

Figure 1 Equivalent circuit for a Debye dielectric relaxation. G_0 is the zero frequency conductance, and C_0 the high frequency limiting capacitance. The relaxation behavior is simulated by the series conductance and capacitance in the lowest arm of the circuit. τ is the dielectric relaxation time.

Figure 2 Spectra of the four basic relaxation functions for a representative equivalent circuit, where ω is the angular frequency in radian $\sec^{-1}$. Single primed symbols refer to real components, double primed symbols to imaginary components.
(A) Equivalent circuit.
(B) Spectra of the components of the complex conductivity σ^* . The high and low frequency relaxation limits of the real component are shown (σ_∞ and σ_0 respectively). The spectrum of σ'' with its high frequency limit σ_∞ (proportional to ω) subtracted is also shown.
(C) Spectra of the components of the complex relative permittivity ε^*. The spectrum of ε'' with the zero frequency conductivity contribution $\sigma_0/\mathrm{e}_0\omega$ subtracted out, is also shown. Note the logarithmic scale for ε^* at low frequencies, and linear scale at high frequencies.
(D) Spectra of the components of the complex resistivity ρ^*. Logarithmic scales are given in the insets to indicate the presence of the high frequency peak in ρ'' at low frequencies.
(E) Spectra of the components of the complex electric modulus, *M**. The non-zero low frequency limit of *M'* is shown at left.

Figure 3 Complex plane plots for the circuit and spectra of Figure 2.
(A) Complex conductivity plane. The low frequency relaxation due to C_s is shown in the inset (note different scale).
(B) Complex relative permittivity plane. Note the different scales for the low frequency (upper) and high frequency (lower) relaxations.
(C) Complex resistivity plane. Note different scales for each part.
(D) Complex modulus plane.

Figure 4 Arrhenius plot for conductivity for Li_4GeO_4 at different fixed measuring frequencies. The dotted line gives the expected high temperature behavior (not measured). After ref [57].

Figure 5 Complex admittance plane behavior of polycrystalline yttria-zirconia solid electrolytes, after Bauerle [37].
(A) Equivalent circuit used in data processing.
(B) Complex admittance plane for circuit given in (A). The relations between the complex plane parameters and the circuit elements are given at the bottom of the figure.
(C) Experimental complex admittance plane behavior. Each relaxation conforms to the Cole-Cole function (see Appendix A2-3). The angles θ measure the displacement of the semicircle centers below the real axis and are related to the width parameter α $\left(\alpha = \theta / 90^{\circ}\right)$. Four terminal (4T) and direct current (dc) data are indicated. The upper numbers refer to the measuring frequency in Hz.

Figure 6 Relaxation functions for the proton conducting glass $HZnC1_3 \cdot 4H_20$ at -105°C (Ref. 45).
(A) Spectra of the specific conductivity σ', relative permittivity ε' and electric loss modulus M''. Circles are data points, and solid lines are for the best fit Davidson-Cole function for M''. Davidson-Cole parameters (see Appendix A2-1) are $M_\infty = 0.105$, $\gamma = 0.33$, $\tau_0 = 1.07 \times 10^{-3}$ sec.
(B) Resistivity spectrum. Solid line is spectrum derived from Davidson-Cole function for M''. Circles are observed data points and the dotted line is hand-drawn through the data.
(C) Complex resistivity plane plot. The solid semicircle is calculated from the Davidson-Cole function for M''. The low frequency polarization extrapolation is also shown.

Figure 7 Spectra for single crystal and polycrystalline $\beta-$ alumina at −160°C (after Ingram et al. , refs. [48, 60-62].
(A) Electric loss modulus spectra for single crystal in orientations parallel and perpendicular to conduction plane.
(B) Dielectric loss spectra for single crystal in same orientations as (A).
(C) Electric loss modulus and impedance spectra for single crystal. Open circles are M'' parallel to conduction planes, closed circles are M'' in the perpendicular orientation, and dotted line is Z'' in the parallel orientation.
(D) Electric loss modulus and impedance spectra for polycrystalline $\beta-$ alumina (ref. [48]). Note the coincidence of two resolvable modulus peaks with the crystal spectra for the two orientations shown (A).

Figure 8 Complex impedance plane data at room temperature for 2 sintered polycrystalline $\beta-$ alumina preparations (after Armstrong et al, Ref. 20).
(A) Sinter 1 (see Ref. 20 for preparation details).
(B) Sinter 2, with different surface preparations. Note that the high frequency extrapolations give self-consistent values for σ_0.

Figure 9 Complex impedance plane plots for KHF_2 (after Bruinink Ref. 54).
(A) Single crystal $\alpha-KHF_2$, in an atmosphere of H_2.
(B) Single crystal $\alpha-KHF_2$, in vacuo. Inset gives the low frequency relaxation due to electrode polarization.
(C) Polycrystalline $\alpha-KHF_2$.

Figure 10 Relaxation spectra for a cracked and an annealed polycrystalline preparation of a lithium ion solid electrolyte (after Hodge et al, ref. [41]).
(A) Impedance and modulus spectra for the indicated equivalent circuit.
(B) Modulus spectra of cracked (1), partially annealed (2), and fully annealed (3) material.
(C) Impedance spectra corresponding to data given in (B). Note the disappearance of the low frequency relaxation with annealing. The dotted lines are a resolution assuming the low frequency relaxation to be symmetric.
(D) Conductivity spectra corresponding to data given in (B) and (C). Note the great loss of information compared with the spectra given in C.

Figure 11 Relaxation spectra for polycrystalline zinc oxide in 1 atm O_2 (after Seitz and Sokoly, ref. [58]). Note logarithmic ordinate scales. Circles are data points at 500 K. Dotted line in inset is permittivity spectrum at 800 K.

Figure 12 Temperature dependences of dielectric loss spectra (A) and electric loss modulus spectra (B) of water droplets in heptane-$CC1_4$ emulsions (after Hodge and Angell, ref. [69]). Open and closed circles and open and closed squares are data at 0°, -9.8°, -21.4° and -35.0°C, respectively.

Figure 13 Relaxation functions in the temperature domain for $Ca(NO_3)_2.4H_2O$ at 1 Hz (after Hodge and Angell, Ref. 24).

Figure 14 Electric loss moduli versus reciprocal temperature for a series of glassy Li salt/acid mixtures, illustrating the masking of the secondary relaxation in Li salt by the conductivity of the acid (Ref. 45). Inset: The same data as a function of E_A / RT, where E_A is the average activation energy for the (high temperature) conductivity relaxation. Δ denotes shifts of spectra to make the conductivity relaxations coincide.

Figure A2-1 Definition of electric loss modulus parameters.

Figure A2-2 Comparison of Cole-Cole resistivity spectrum (closed circles) with the spectrum derived from Davidson-Cole M'' spectrum (open circles). Note the two frequency scale corresponding to shifts made to make half height points coincide. The Cole-Cole function has been normalized to make ρ''_{max} coincide with that of the Davidson-Cole function.

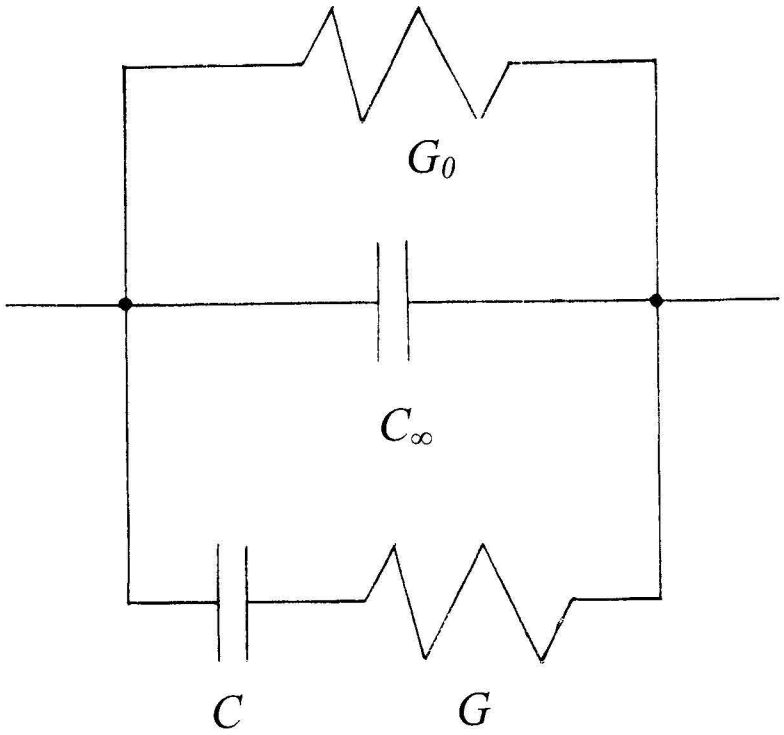

$$\tau = C_\infty / G_0$$

Figure 1

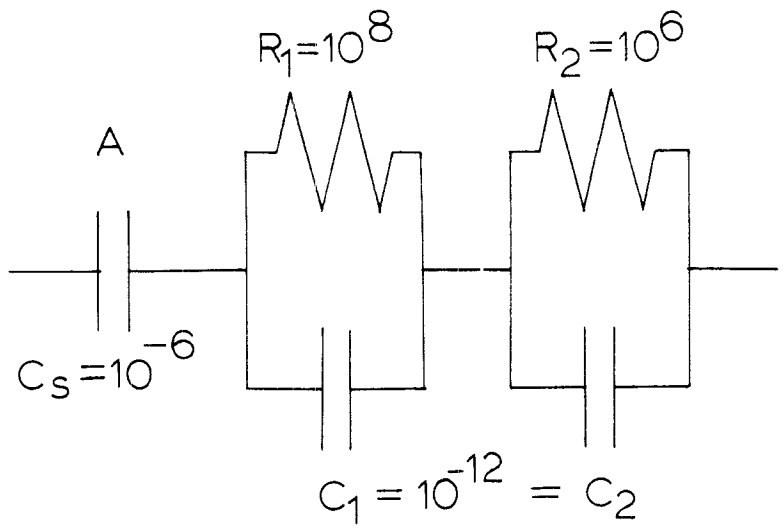

Figure 2A

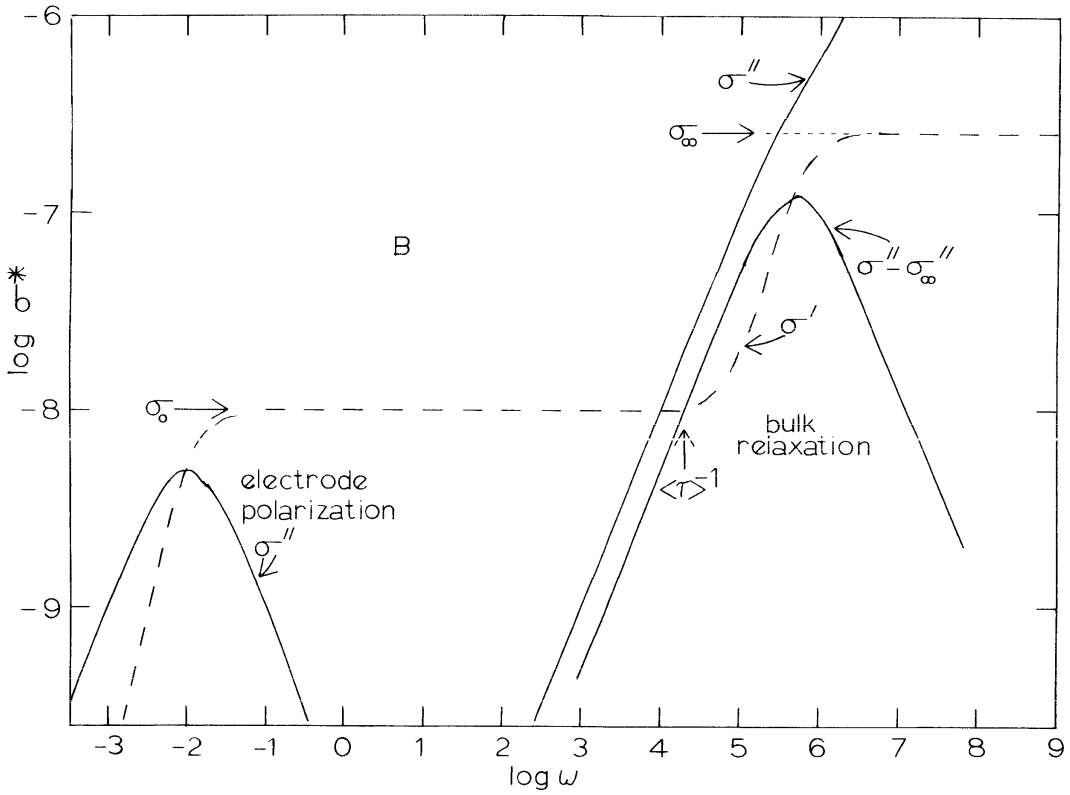
-6
-7
-8
-9
log σ*
B
σ''
σ∞
σ''-σ∞''
σ'
σ₀
electrode
polarization
σ''
bulk
relaxation
<τ>⁻¹
-3
-2
-1
0
1
2
3
4
5
6
7
8
9
log ω

Figure 2B

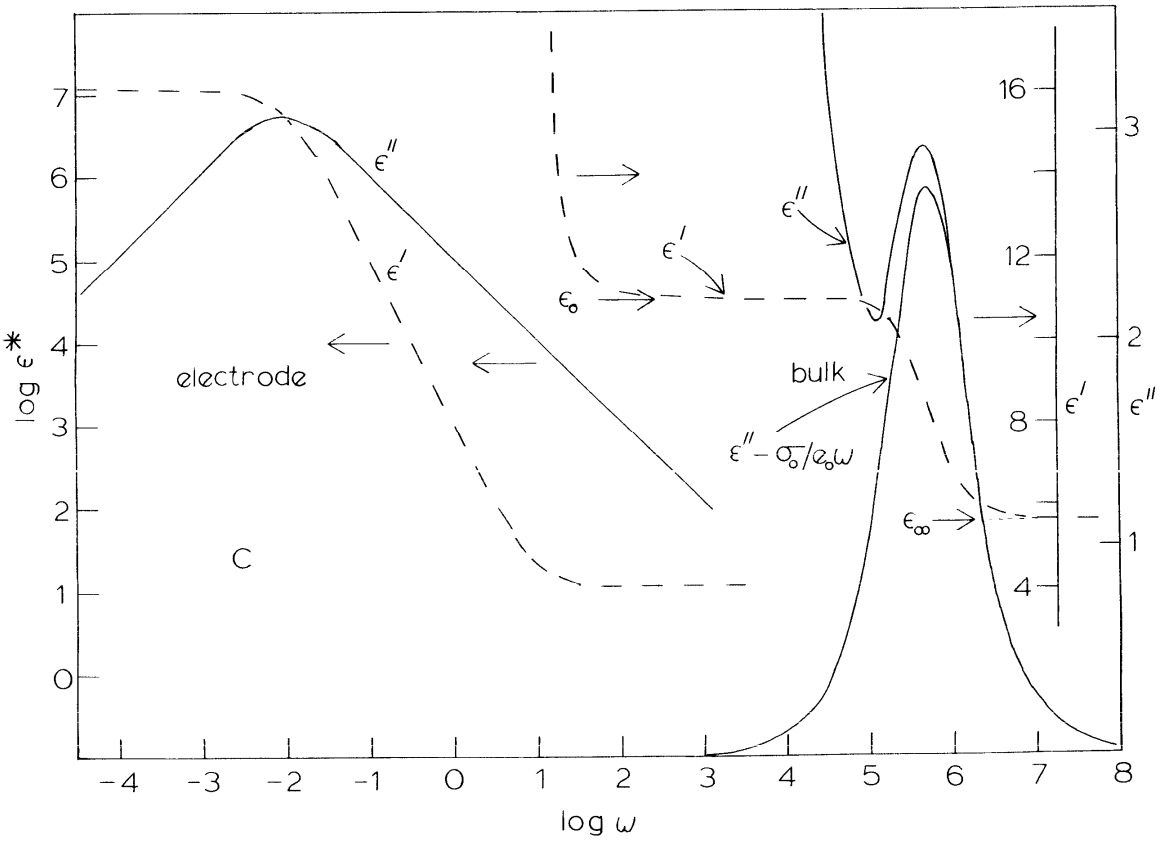

Figure 2C

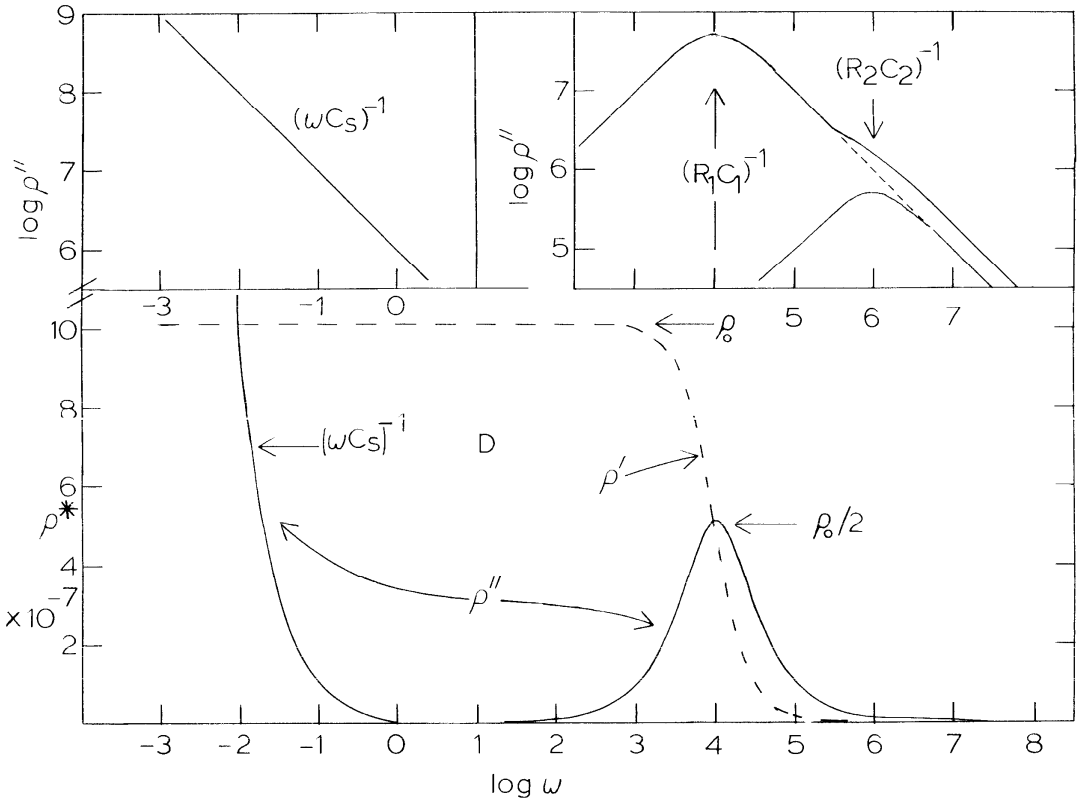

Figure 2D

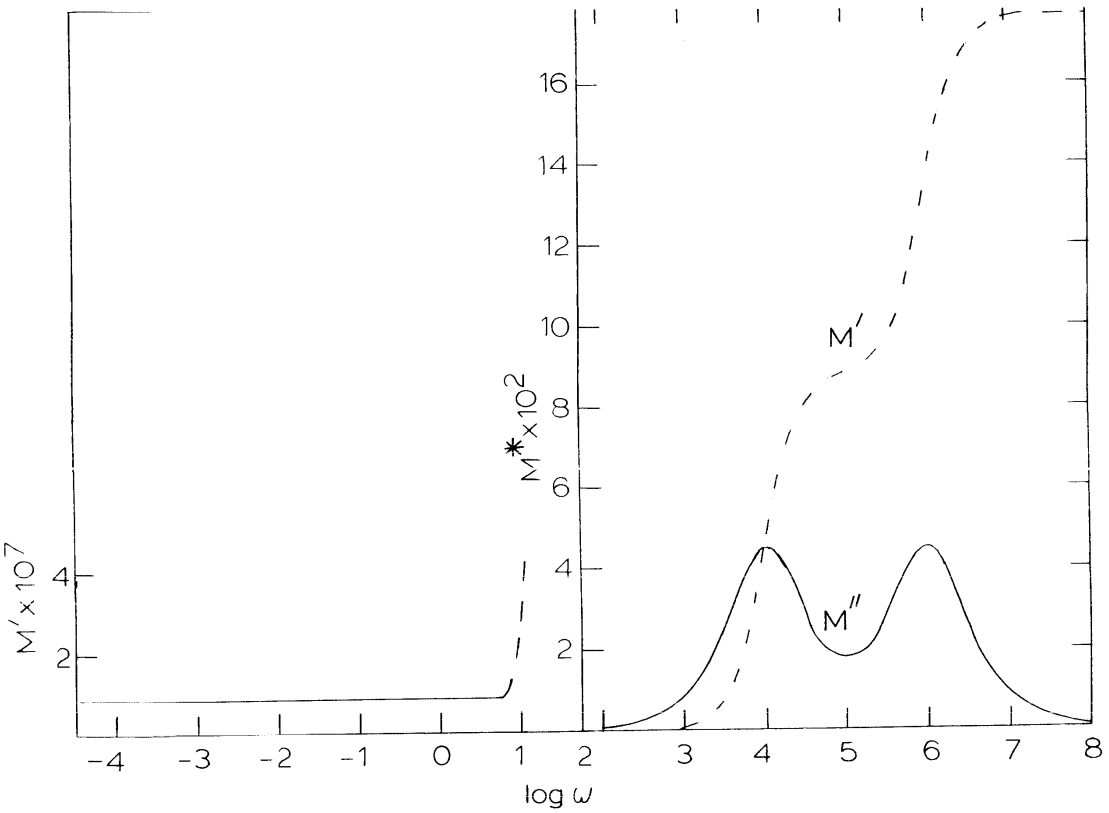

Figure 2E

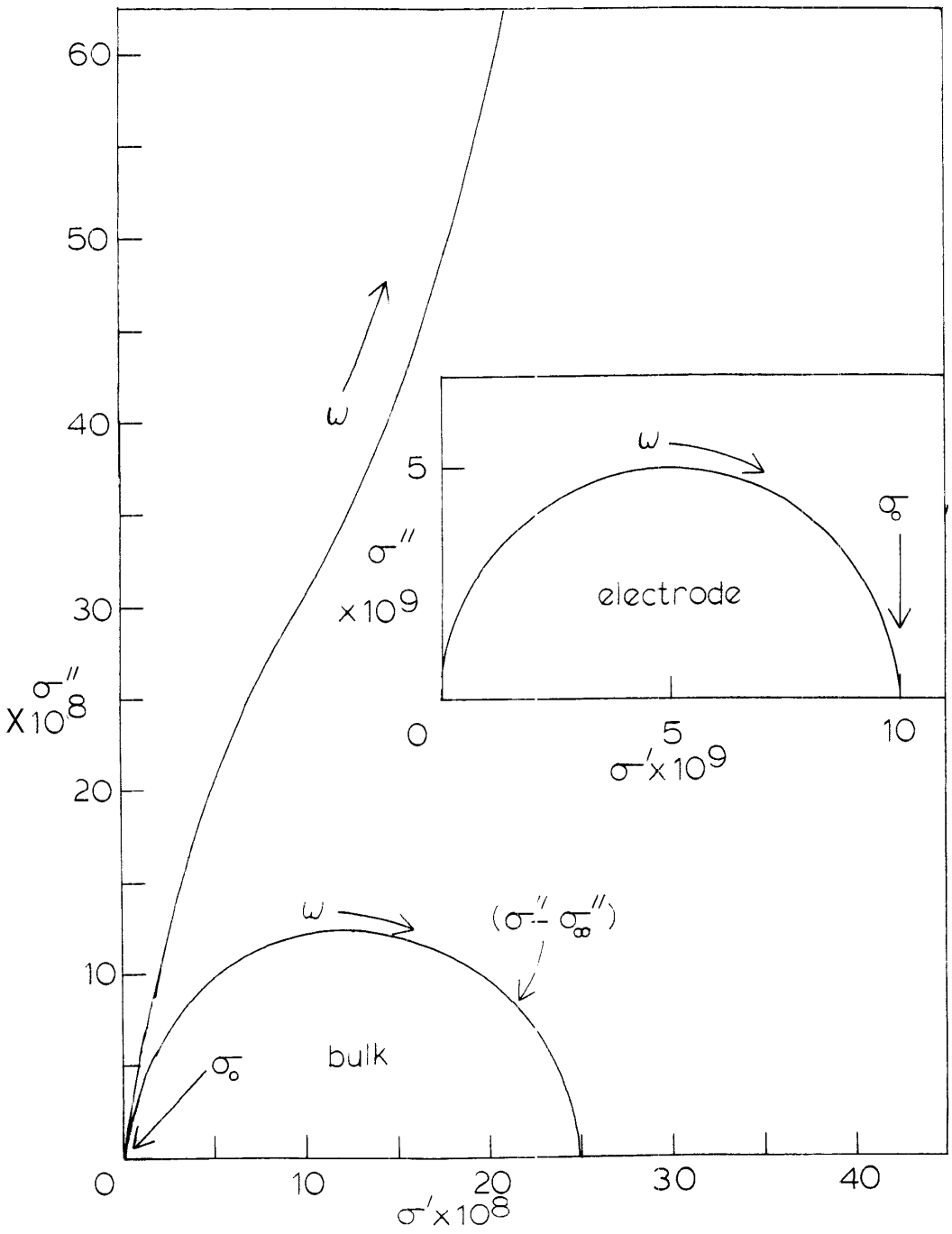
60
50
40
30
20
10
0
10
20
30
40
σ″ X10^8
σ′ x 10^8
ω
σ₀
bulk
(σ′ − σ₈″)
5
0
5
10
σ″ x 10^9
σ′ x 10^9
ω
σ₀
electrode

Figure 3A

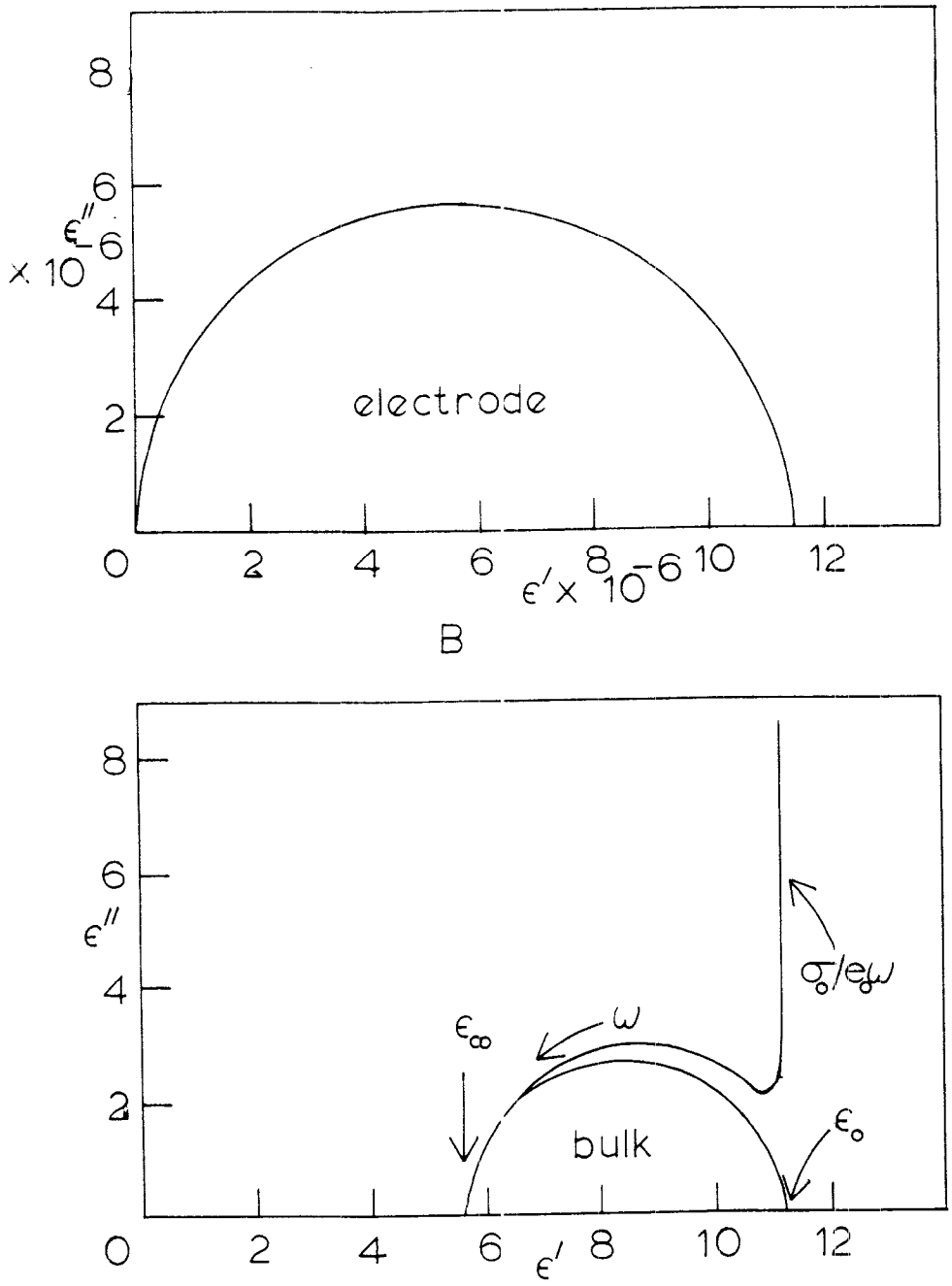
8
6
4
2
0
2
4
6
8
10
12
ϵ''
$\times 10^{-6}$
$\epsilon' \times 10^{-6}$
electrode
B
ϵ''
ϵ_∞
ω
$\sigma_0/e_0\omega$
bulk
ϵ_0
ϵ'

Figure 3B

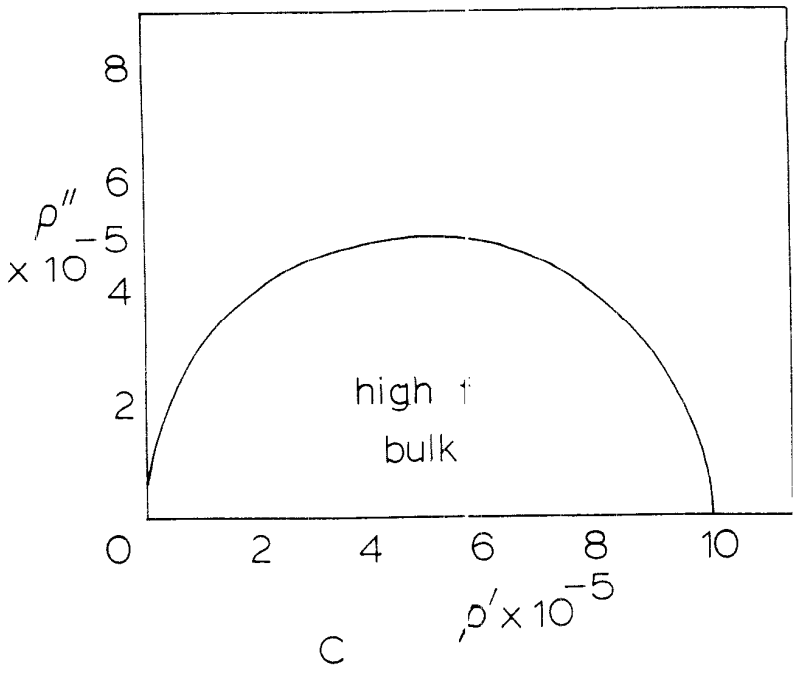
8
6
ρ''
x 10^-5
4
2
high f
bulk
0
2
4
6
8
10
ρ' x 10^-5
C

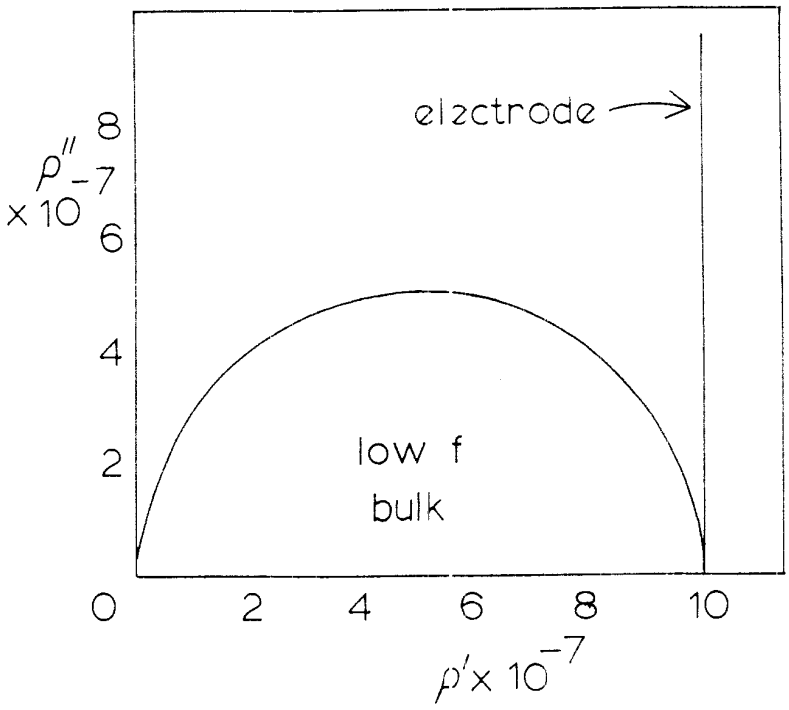
electrode
8
ρ''
x 10^-7
6
4
2
low f
bulk
0
2
4
6
8
10
ρ' x 10^-7

Figure 3C

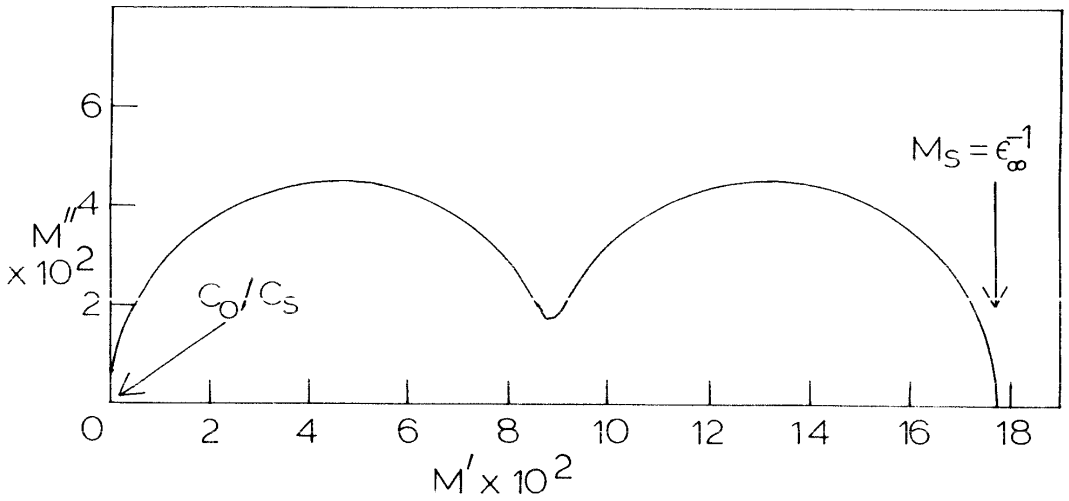

Figure 3D

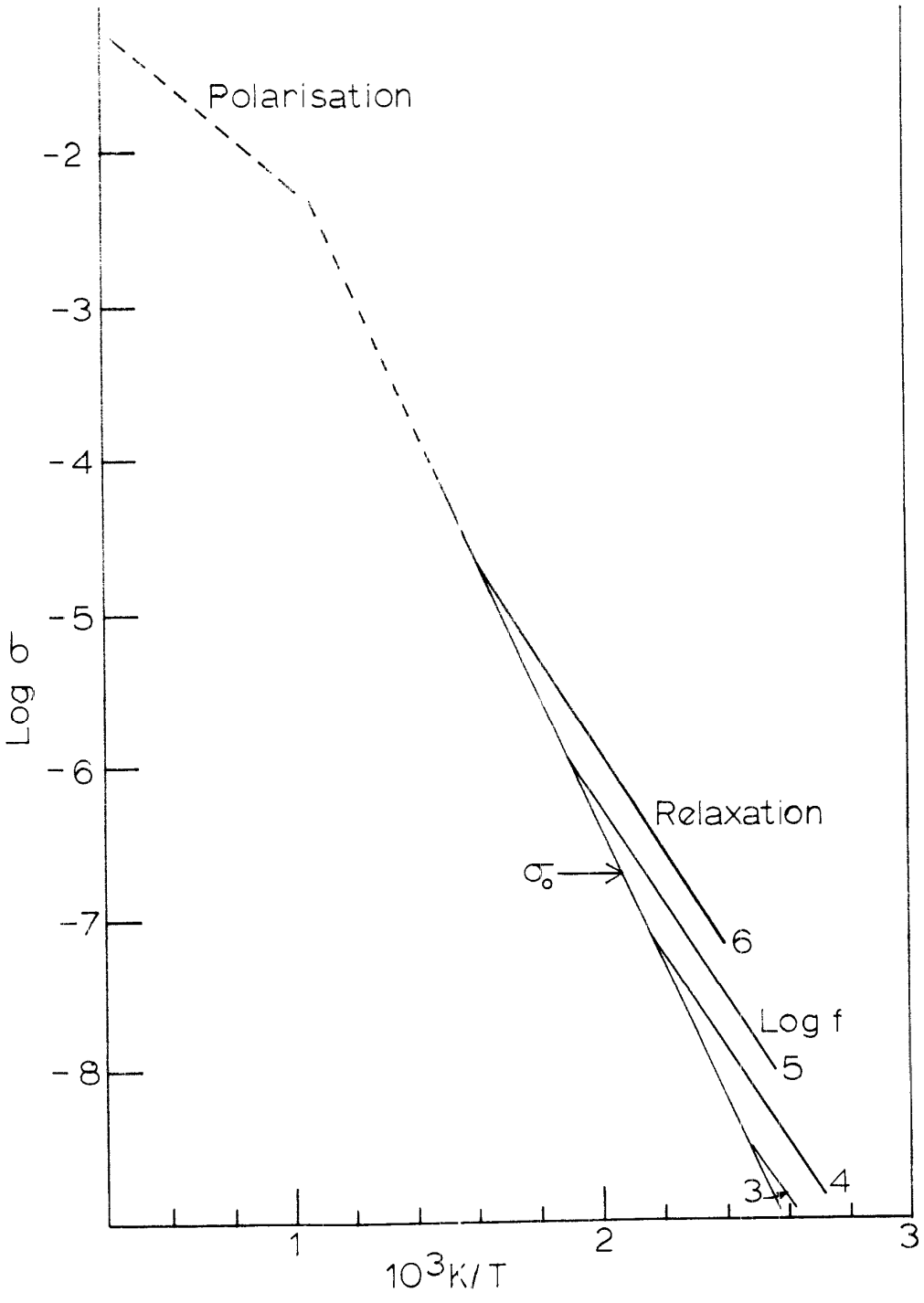
Polarisation
-2
-3
-4
-5
-6
-7
-8
Log σ
Relaxation
σo
6
Log f
5
4
3
1
2
3
10³K/T

Figure 4

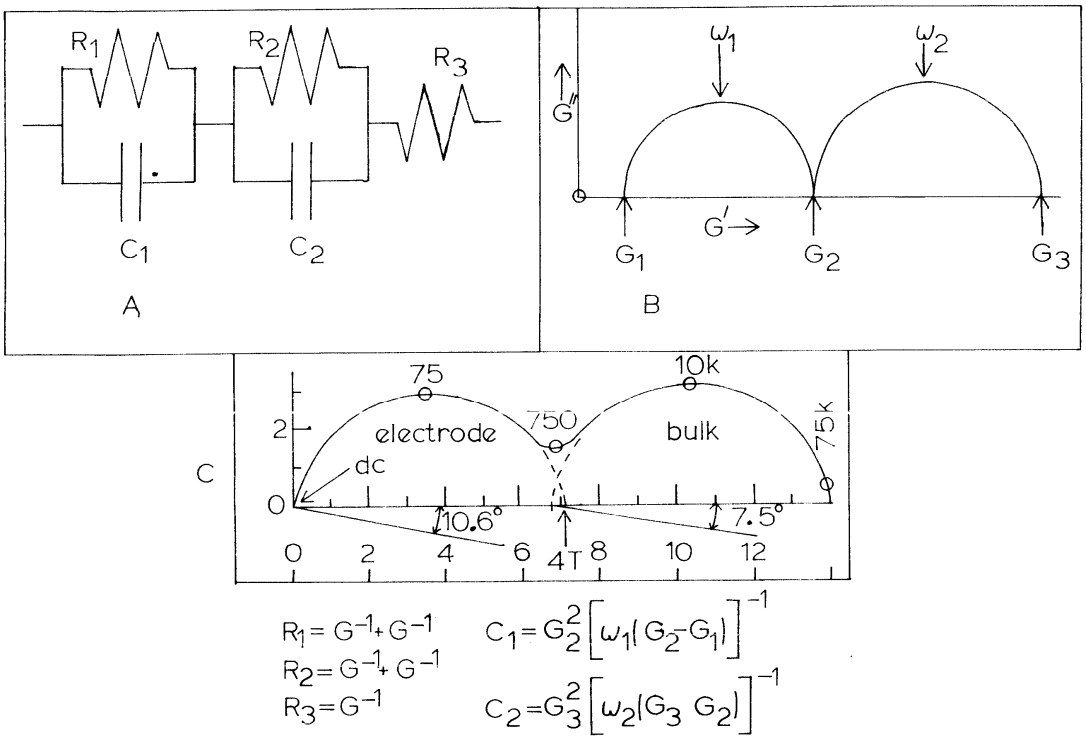
R1
R2
R3
C1
C2
A
ω1
ω2
G''
G'
G1
G2
G3
B
C
75
10k
2
electrode
750
bulk
75k
dc
0
10.6°
7.5°
0 2 4 6 4T 8 10 12
R1 = G⁻¹ + G⁻¹
R2 = G⁻¹ + G⁻¹
R3 = G⁻¹
C1 = G2² [ω1(G2 − G1)]⁻¹
C2 = G3² [ω2(G3 G2)]⁻¹

Figure 5

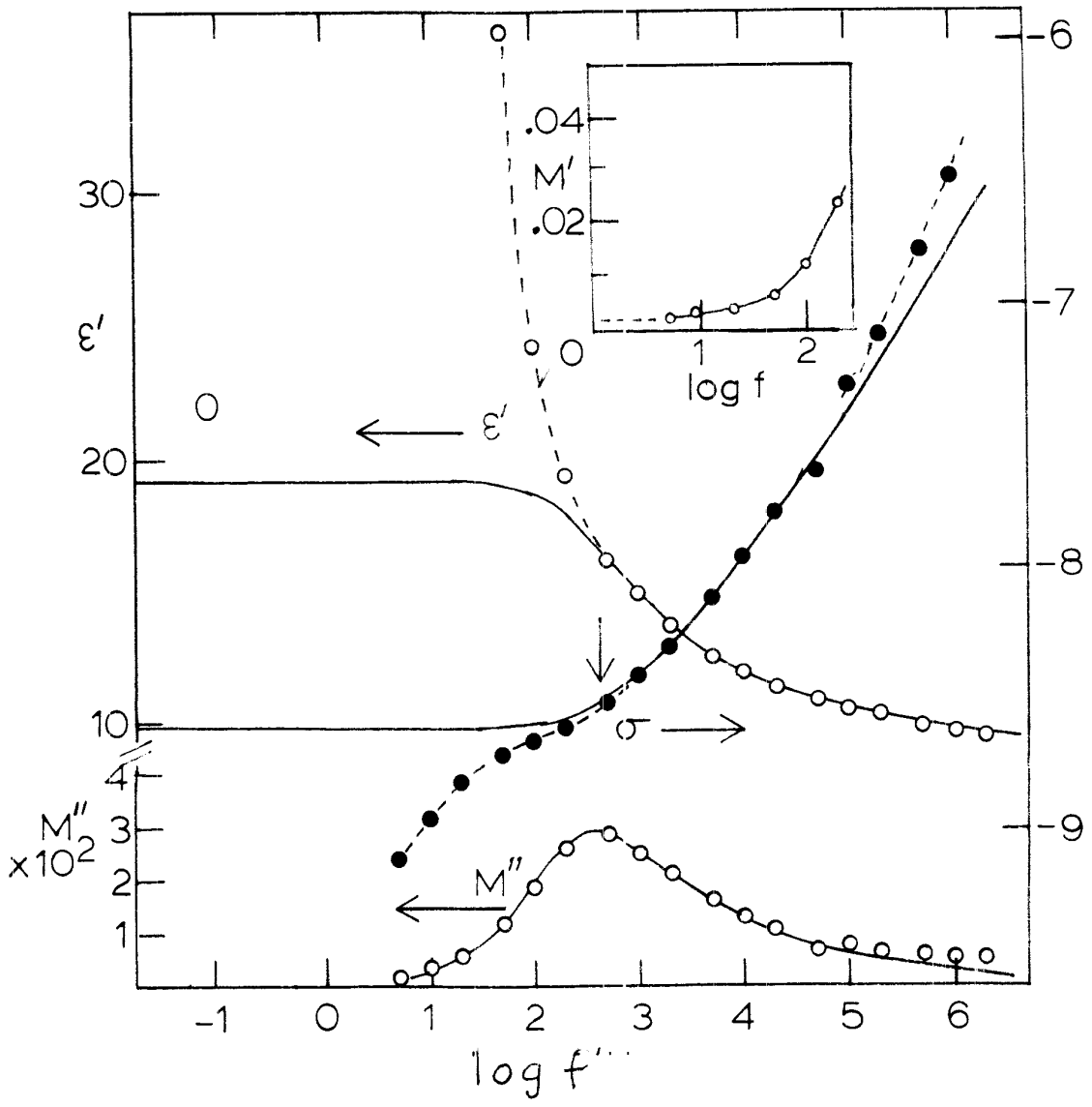

Figure 6A

Figure 6B

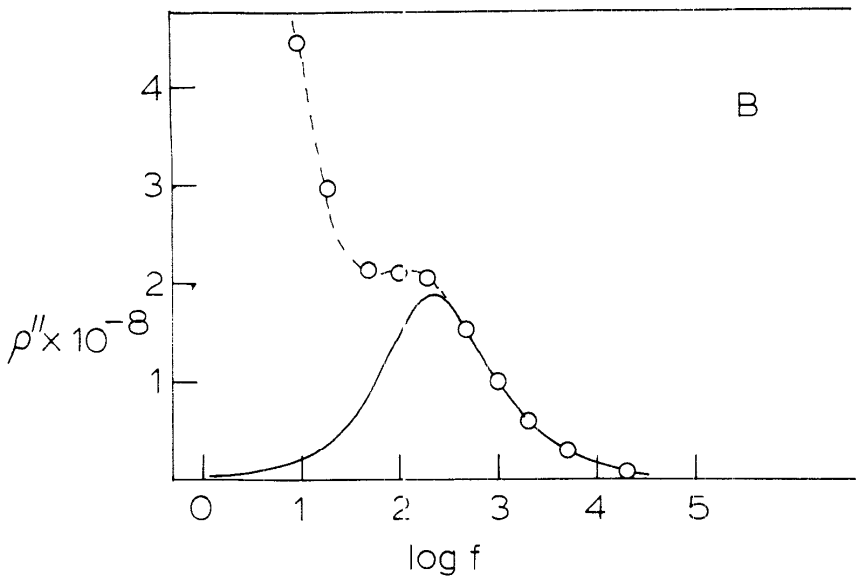

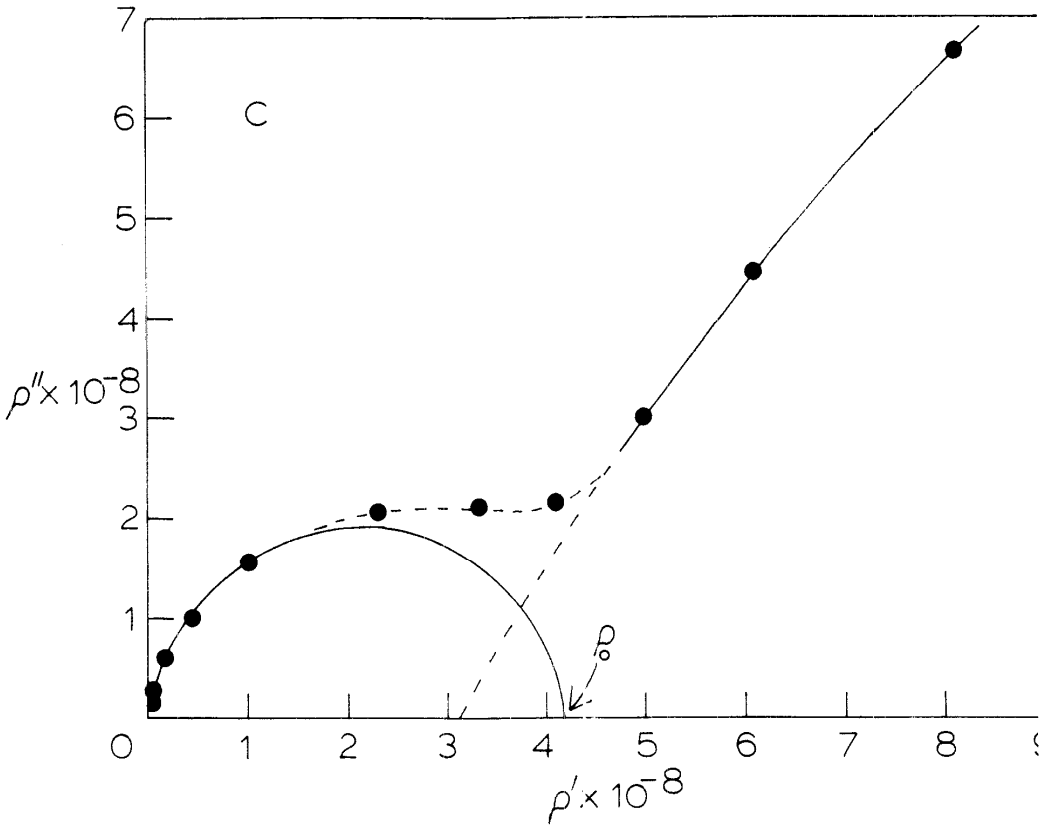

Figure 6C

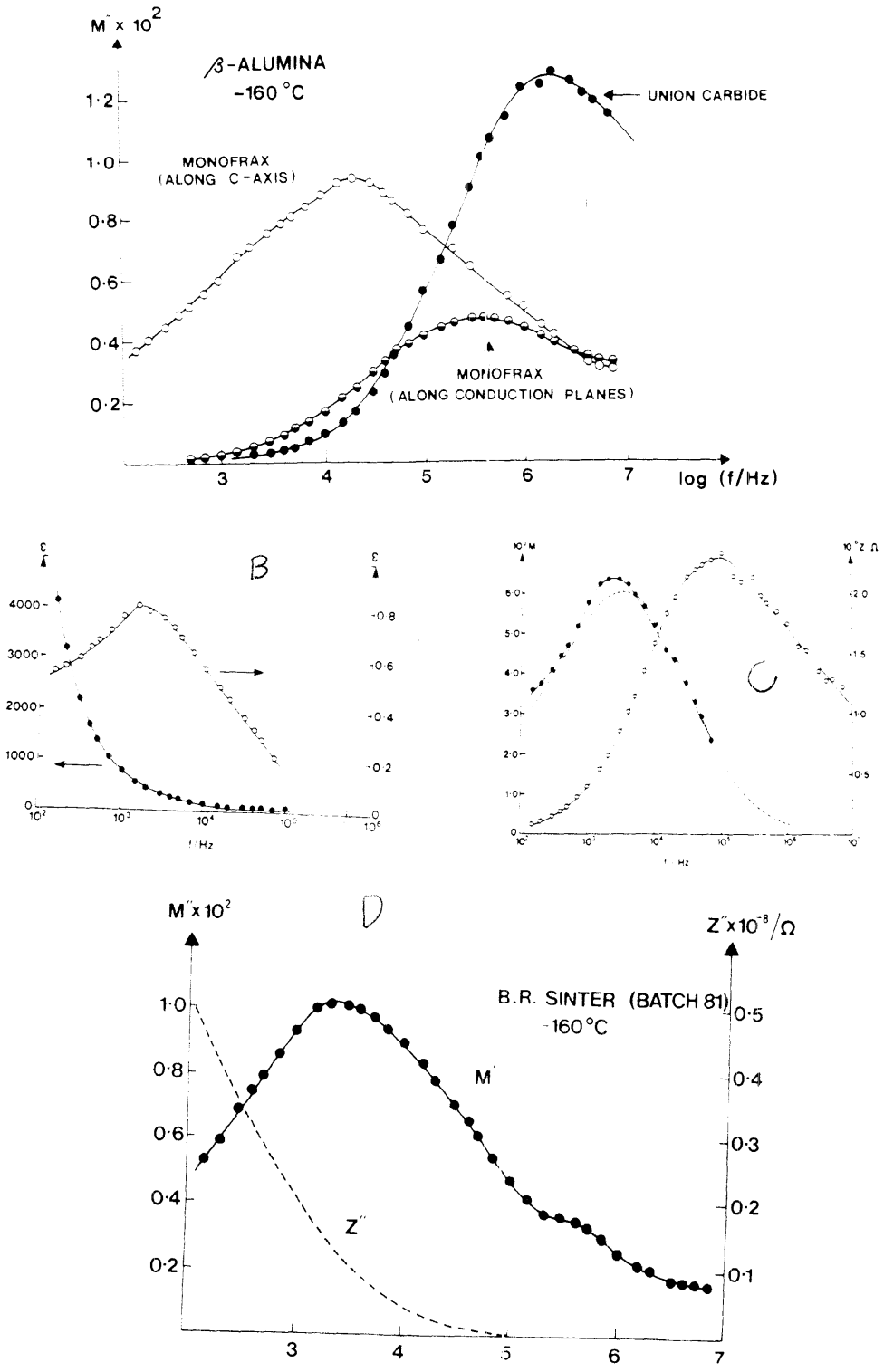
M'' x 10^2
β-ALUMINA
-160 °C
UNION CARBIDE
MONOFRAX
(ALONG C-AXIS)
MONOFRAX
(ALONG CONDUCTION PLANES)
log (f/Hz)
B
C
D
M''x10^2
Z''x10^-8/Ω
B.R. SINTER (BATCH 81)
-160 °C
M'
Z''

Figure 7

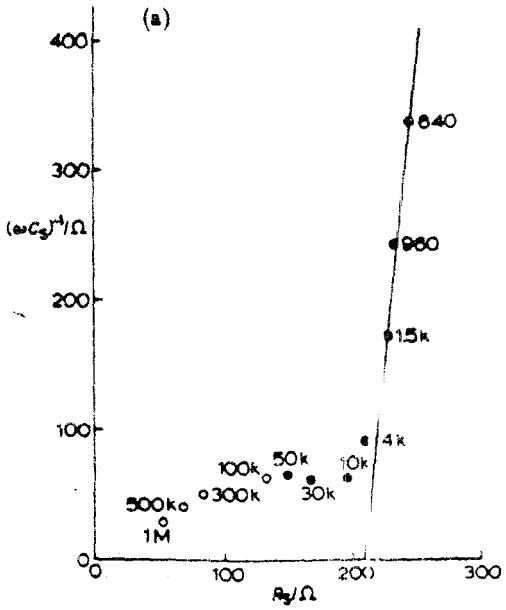

A

Fig. 8. The impedance of β''-alumina sinter 1. (a) At room temperature

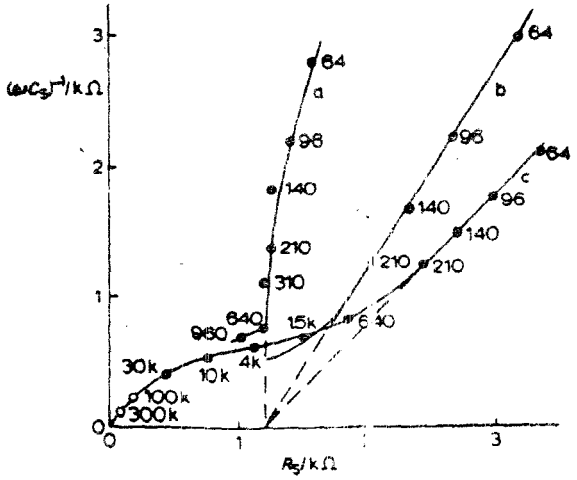

B

Fig. 9. The impedance of β''-alumina sinter 2 at room temperature showing the effect of different surface preparations.

Figure 8

A

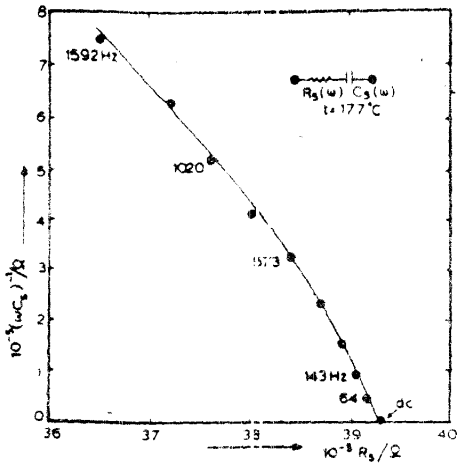
1592 Hz
1020
573
143 Hz
64
dc
$R_s(\omega)$ $C_s(\omega)$
$10^{-8} R_s/\Omega$

B

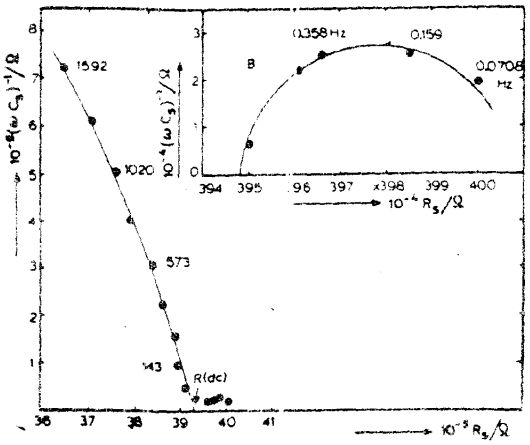
1592
1020
573
143
R(dc)
0.1358 Hz
0.159
0.0708 Hz
B
$10^{-5} R_s/\Omega$
$10^{-4} R_s/\Omega$

C

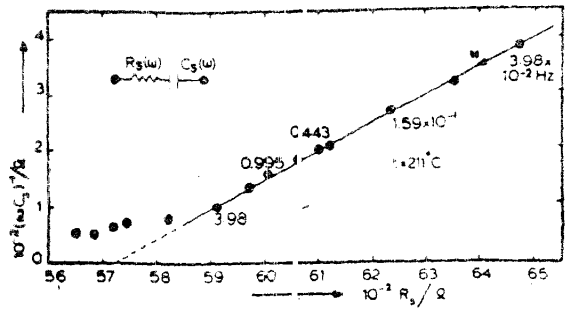
$R_s(\omega)$ $C_s(\omega)$
3.98
0.995
0.443
1.59×10^{-1}
3.98×10^{-2} Hz
$10^{-2} R_s/\Omega$

Figure 9

A

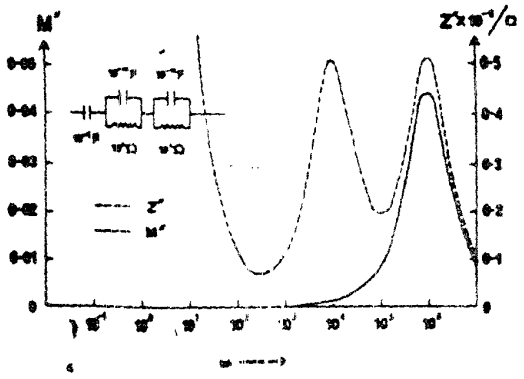

B

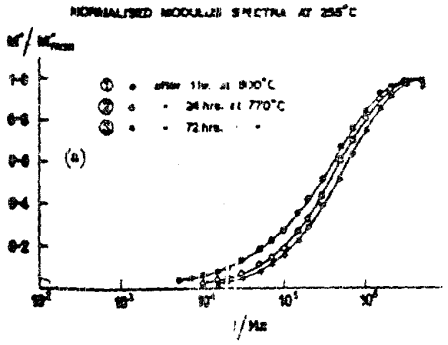

C

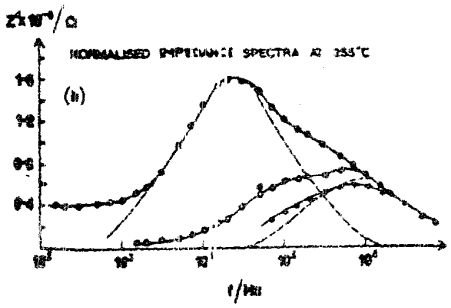

D

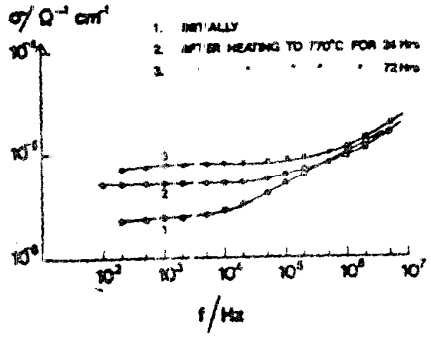

Figure 10

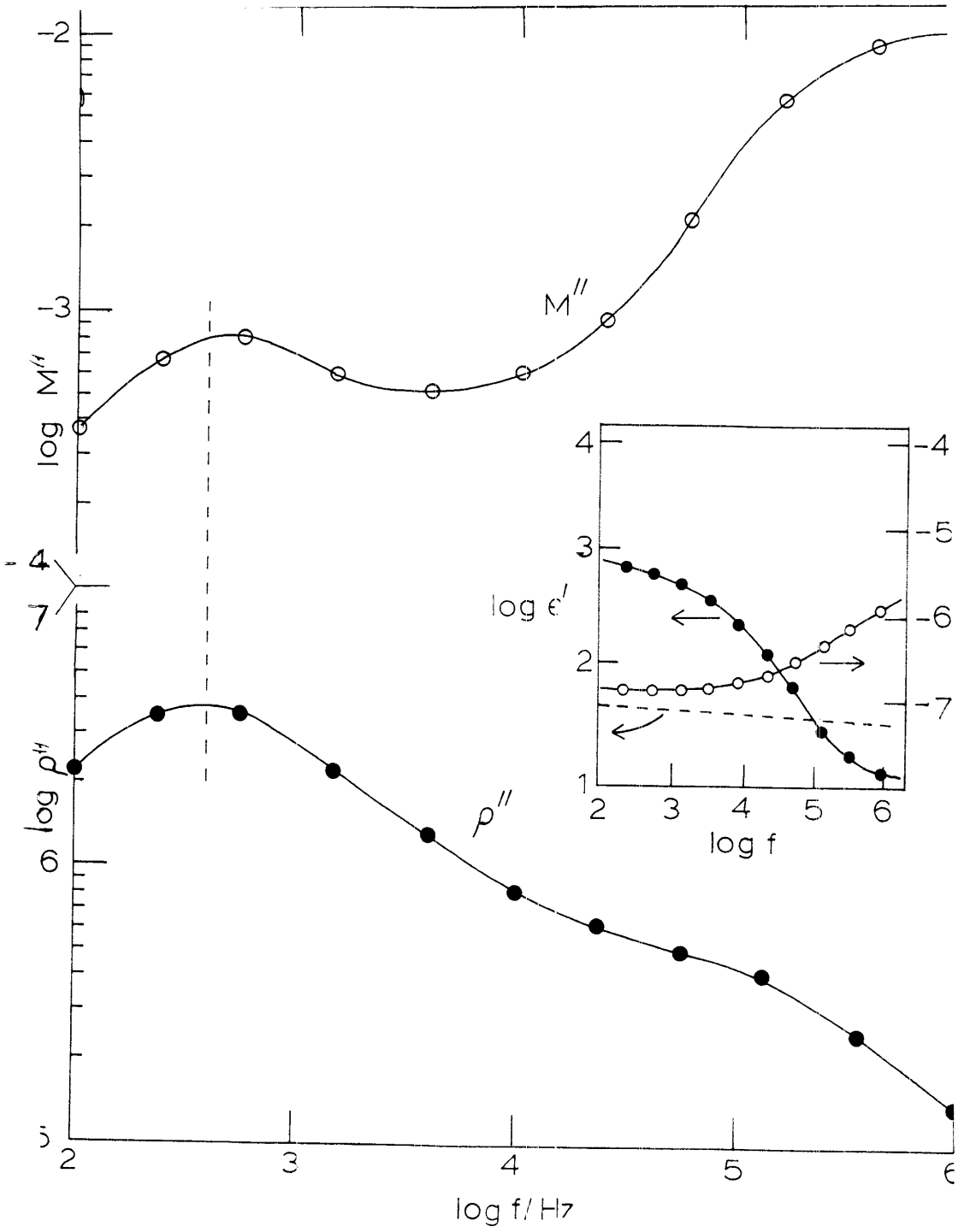

Figure 11

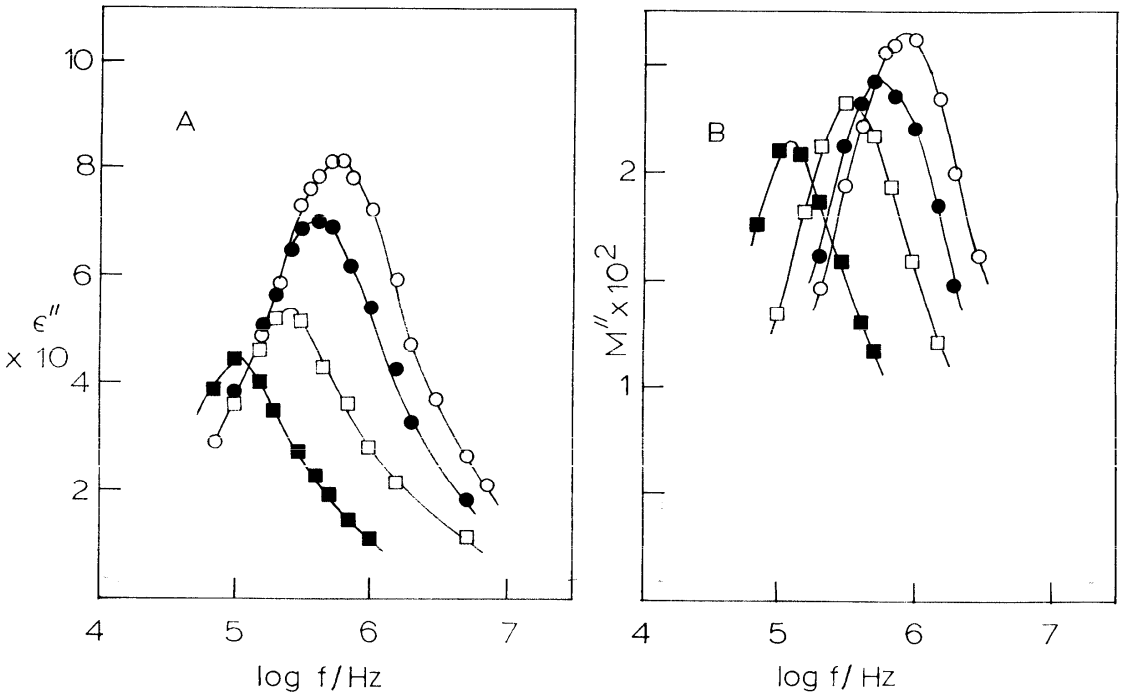

Figure 12

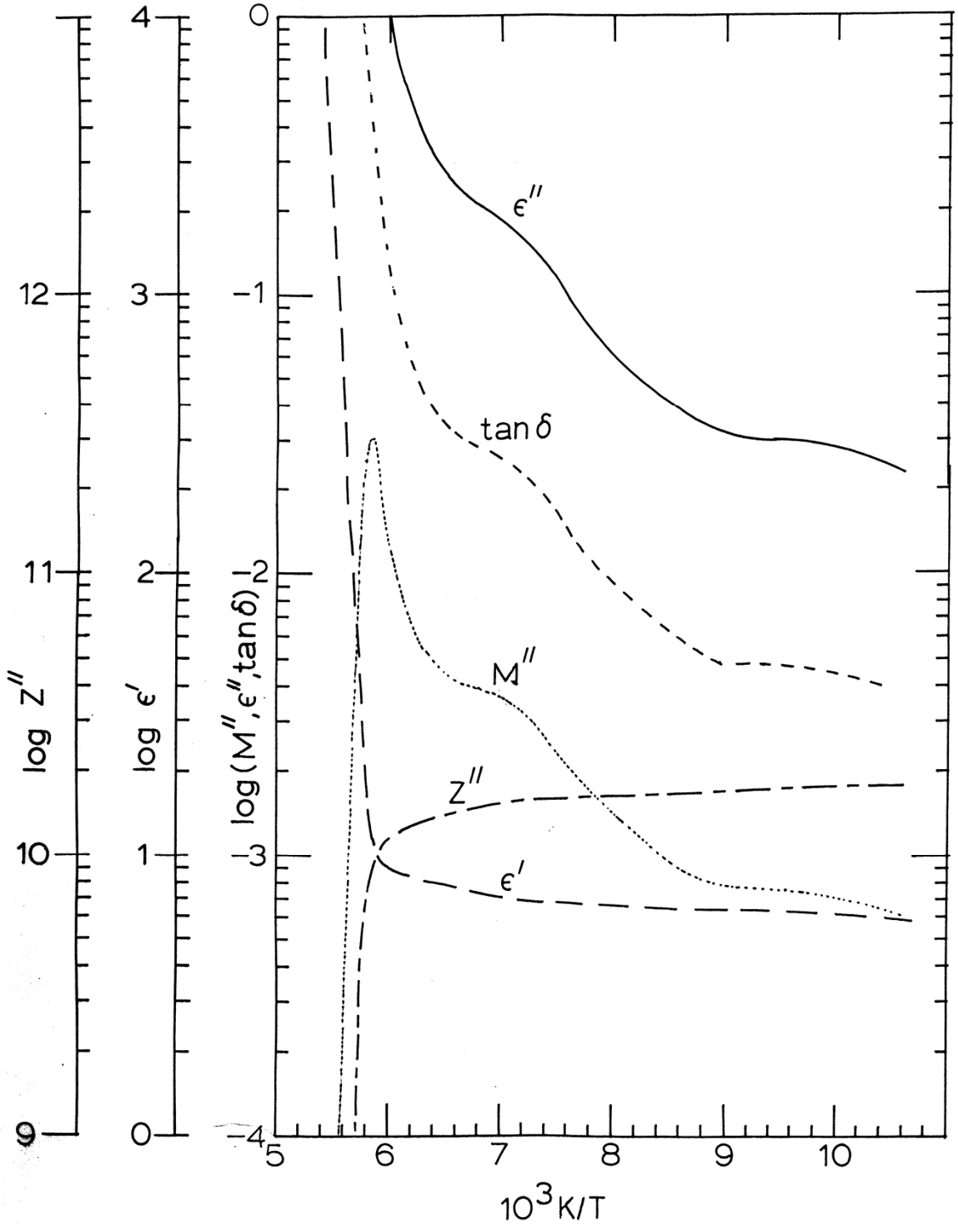

FIGURE 13

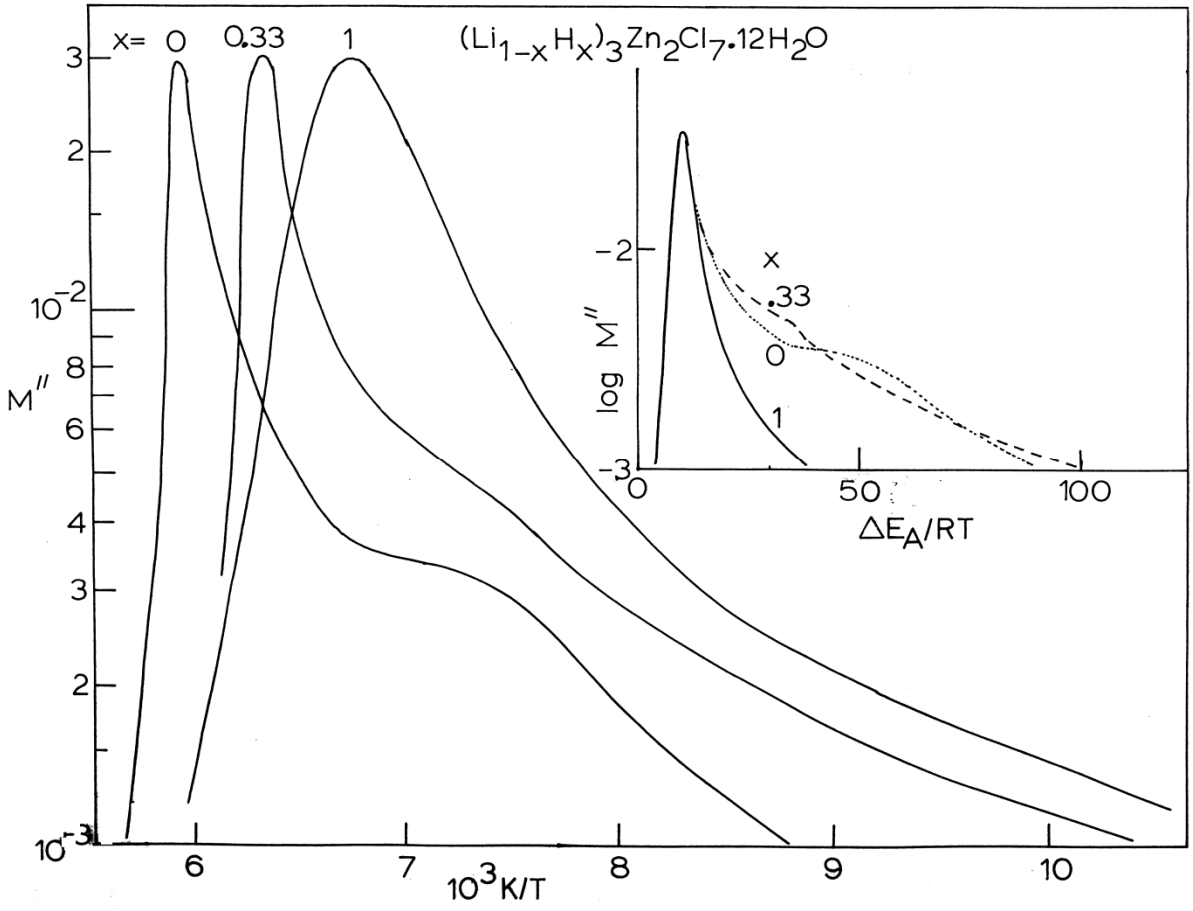
x= 0 0.33 1
$(Li_{1-x}H_x)_3Zn_2Cl_7 \cdot 12H_2O$
M''
10^{-2}
10^{-3}
3
2
8
6
4
3
2
6
7
8
9
10
10^3 K/T
log M''
-2
-3
x
.33
0
1
0
50
100
$\Delta E_A/RT$

FIGURE 14

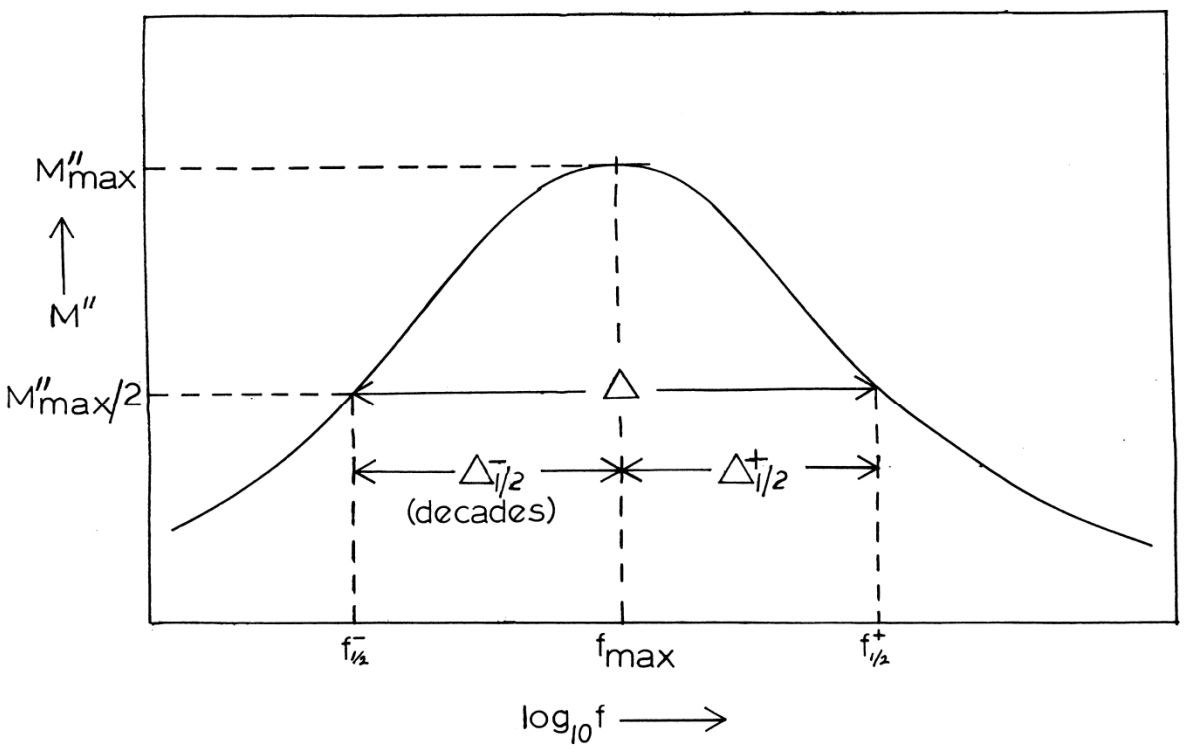

FIGURE A2.1

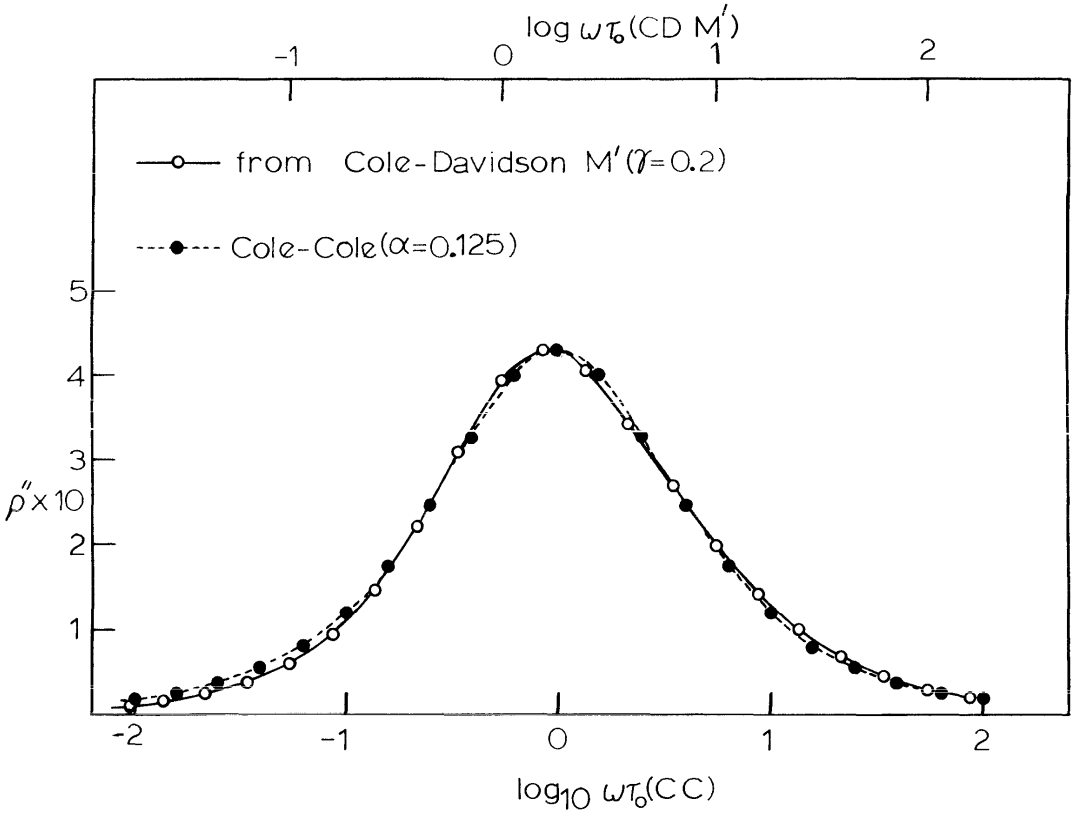
log ωτ₀(CD M′)
-1
0
1
2
from Cole-Davidson M′(γ=0.2)
Cole-Cole(α=0.125)
5
4
3
ρ″x10
2
1
-2
-1
0
1
2
log₁₀ ωτ₀(CC)

Figure A2.2

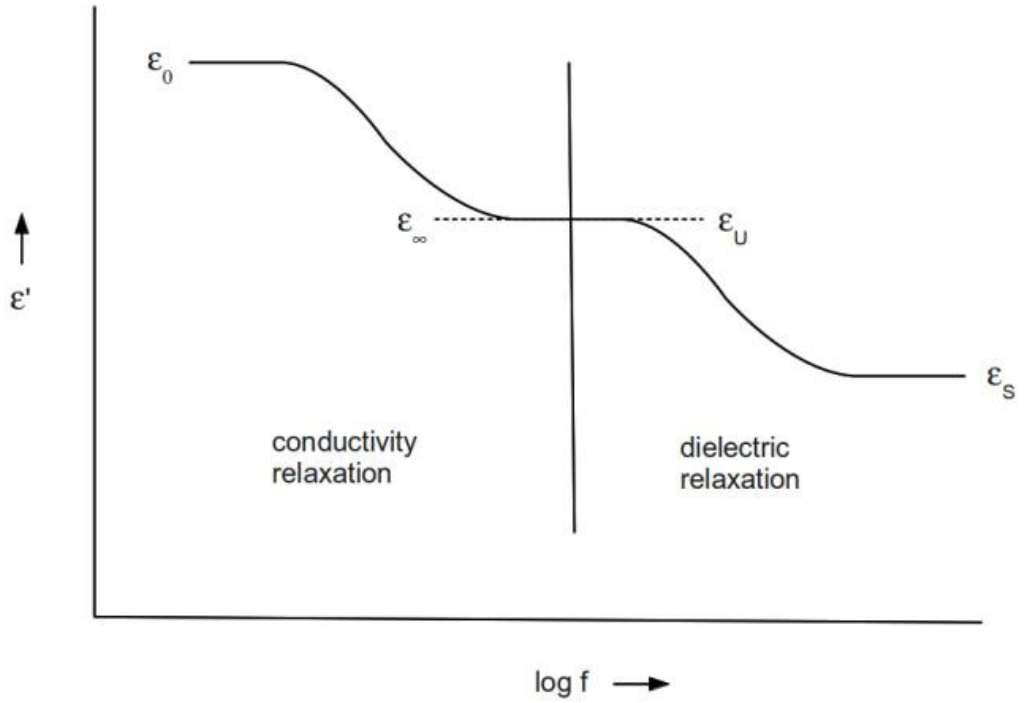
ε0
ε∞
εU
εS
ε'
conductivity
relaxation
dielectric
relaxation
log f

Figure A3